

a

PROJEKTARBEIT / STUDENT PROJECT

THREE DIMENSIONAL DUAL COLOUR
SINGLE MOLECULE LOCALISATION
FLUORESCENCE MICROSCOPY

concluded at the

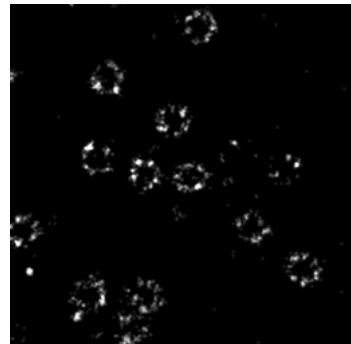
TECHNISCHE UNIVERSITÄT (TU) WIEN

advised by

LUKAS VELAS

of

MORITZ SIEGEL



Vienna
February 5, 2023

moritz.siegel@tuwien.ac.at
<https://github.com/imrahilias/biophysics>

Contents

1	Introduction	5
1.1	Fluorescence	5
1.2	Fluorescence Microscopy	6
1.3	Total Internal Reflection	7
1.4	Single Molecule Localisation	7
1.5	Two Dimensional SMLM	8
1.6	Three Dimensional SMLM	8
2	Methods	9
2.1	Maximum Likelihood	9
2.2	PSF Model & Zernike	9
2.3	STORM & dSTORM	9
2.3.1	Gloxy Buffer	9
2.3.2	OxEA Buffer	10
2.4	Dual Colour Optics	10
2.4.1	Aberration Correction Collar	10
2.4.2	Cramér Rao Lower Bound	11
2.5	Dual Colour Projection	11
2.5.1	Rigid Transform	11
2.5.2	Affine Transform	11
2.5.3	Simulation	12
2.5.4	Projected 2d NPC	12
3	Results	14
3.1	Dual Colour Buffer	14
3.2	Dual Colour Optics	15
3.2.1	Zernike Modes	15
3.2.2	Cramér Rao Lower Bound	21
3.3	Two Dimensional SMLM	25
3.4	Three Dimensional SMLM	27
3.4.1	Import	27
3.4.2	Drift Correction	27
3.4.3	Photon Counts	27
3.4.4	Filter	27

3.4.5	Track Particles	28
3.5	NPC Analysis	29
3.5.1	Clustering	29
3.5.2	Cluster Analysis	29
3.5.3	Select Clusters	30
3.5.4	X,Y,Z Histograms	30
3.6	Dual Colour 3d SMLM	32
3.6.1	Simulation	32
3.6.2	Projected 2d NPC	35
4	Discussion & Conclusion	37
4.1	Dual Colour Optics	37
4.1.1	Zernike Modes	37
4.1.2	Correction Collar	37
4.2	Three Dimensional SMLM	38
4.3	NPC Analysis	38
4.3.1	Define Scalar Quality	38
4.3.2	Secondary Filter	38
4.4	Dual Colour Buffer	39
4.5	Dual Colour Projection	39
4.5.1	SMLM Simulations	39
4.6	Dual Colour Simulation	39
4.6.1	Projected 2d NPC	40
A	Code	41
A.1	3d SMLM Analysis: NPC	41
A.1.1	Import	41
A.1.2	Drift Correction	42
A.1.3	Photon Counts	42
A.1.4	Filter	42
A.1.5	Track Particles	43
A.2	3d SMLM Analysis: NPC	44
A.2.1	Clustering	44
A.2.2	Cluster Analysis	44
A.2.3	Select Clusters	46
A.2.4	X,Y,Z Histograms	46
A.3	Dual Colour 3d SMLM	48
A.3.1	Cockpit: cockpit.m	48
A.3.2	Splice Channels: ampel.m	50
A.3.3	Rigid Transformation: rig.m	52
A.3.4	Affine Transformation: affine.m	53
A.3.5	Clustering: dbscan.m	55
A.3.6	Simulate Dual Colour 3d SMLM Data: simulate.m	57

Bibliography	60
List of Tables	62
List of Figures	63
Acronyms	65
Index	66

To Do

1. In this section I am missing one figure that would show xy and z(x or y) projection of the NPC to really see if we found the right thing 31
2. index 68

Chapter 1

Introduction

For centuries humans use optical microscopes from magnifying glasses to telescopes to study things smaller than our human eye is able to resolve. Because of electro-magnetic phenomena like interference, using visible light limits the obtainable resolution to about 200 nm—depending which of the two definitions of resolution ABBE or RAYLEIGH is used. Many recent microscope techniques like X-ray microscopy, electron microscopy or atomic force microscopy enable resolutions far beyond optical microscopy. Most of these techniques work fine for solids, but are lethal to living organisms, hence optical microscopy is still ubiquitous in life-science.

The nobel-prize [np1,] awarded technique of single molecule localisation microscopy (SMLM) has become one of many microscope techniques to circumvent ABBE’s diffraction limit, enabling the study of living structures smaller than half the wavelength of light; thus reaching super resolution fluorescence microscopy.

The ultimate goal of this thesis is to facilitate dual colour three dimensional single molecule microscopy, by alternating excitation with different lasers while measuring on the same single channel.

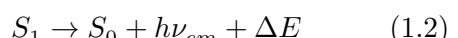
1.1 Fluorescence

The phenomenon of fluorescence exceeds classical optics, thus can only be fully described using quantum mechanics. Here a simplified model is used to explain the concepts necessary for SMLM. Electromagnetic radiation in the form of a photon $h\nu_{ex}$ can be absorbed by a molecule, lifting the molecule from its ground state S_0 to a higher state S_1 —albeit losing some energy ΔE in the form of heat dissipation of excited vibrational states:



where ν_{ex} denotes the *excitation* frequency of the incoming photon, and h the Planck constant.

Some molecules called fluorophores tend to show the opposite reaction immediately after irradiation: The emittance of a fluorescence photon $h\nu_{em}$:



Due to dissipation, the frequency of the emitted photons is lower than those of the initially absorbed photons:

$$\nu_{em} \leq \nu_{ex} \quad (1.3)$$

which leads to the discrimination between RAYLEIGH and STOKES shift:

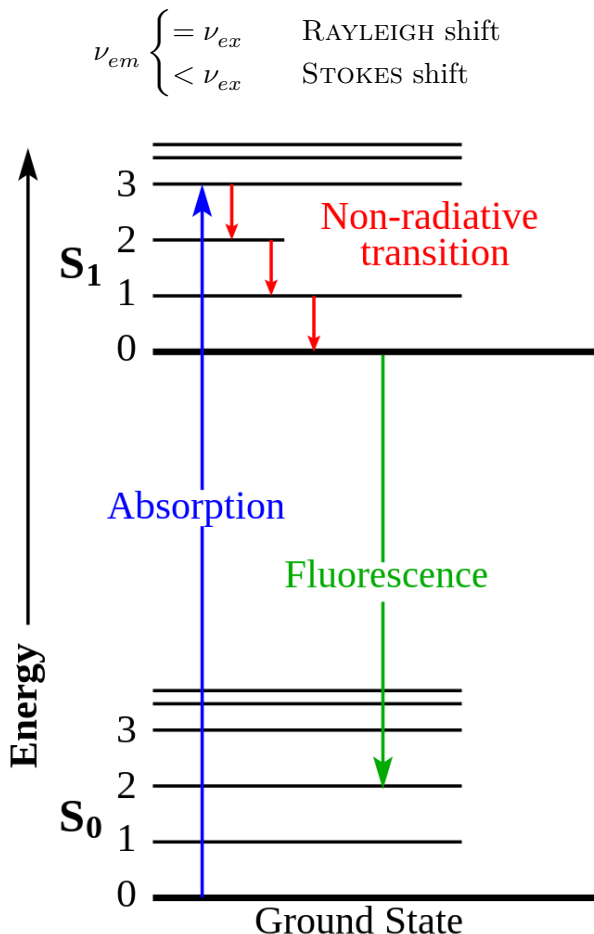


Figure 1.1: Jablonski diagram including vibrational levels for absorbance, non-radiative decay, and fluorescence. Obtained under CC0 license from .

Both processes happen by chance, which leads to the stochastic variables of the rate of a process ρ that we can measure in experiments as occurrence per time, and the lifetime τ of a given state as the time between excitation and emission. An exemplary description is given as a

Many fluorophores have other transition paths that are somewhat rare. Notably is the radiation-free inter-system crossing to a triplet state T_1 . This state may have a long lifetime of up to hours, until it eventually falls

back to ground state. Emitting a much lower energy photon $h\nu$, albeit for a long due the stable nature of the triplet state, this effect was once considered a separate phenomenon termed phosphorescence.

While a fluorophore in its ground state S_0 can shift to its excited state S_1 , a fluorophore in the triplet state could not absorb the same photon to get *back* to the excited state S_1 (at least not of similar energy). It stays dark until it falls back to ground state S_0 .

There are many known issues related to fluorophores, a proper treatment of experimental pitfalls exceed the scope of this work. One of the more frequent issues is called *photo-bleaching*: Some chemical reaction like oxidation might change the molecules characteristics so it loses the ability to fluorescence for good. Some other reaction may re-enable the fluorescence, that is one of the reasons for the use of oxygen-depleted buffers in SMLM.

1.2 Fluorescence Microscopy

Fluorescence microscopy refers to a group of optical microscopy techniques using fluorescence instead of reflection or transmission of light, foremost to study organic substances.

Since most molecules are not showing fluorescence, one needs a way to attach fluorophores to the specimen of question. One widespread example specimen preparation are polystyrene *beads*, that are soaked in a fluorophore solution. When analysing cell constituents, like in our case the *nuclear pore complex*, one must find a way to bind fluorophores to specific structures, like proteins with the use of antibodies. This process is complicated, a detailed explanation would exceed the scope of this paper.

The specimen is illuminated with laser light, exciting the respective fluorophores; causing them to emit (much weaker) light on a slightly

longer wavelength. After separation from excitation light using spectral filters, this image is captured by a sensitive camera like a Electron multiplying charge-coupled device (EMCCD).

The accuracy of fluorescence microscopy heavily relies on the signal-to-noise ratio (SNR) of the emitted light. If it is used to analyse translucent three dimensional structures, like cells, out of focus fluorophores become a problem.

If one would excite all those fluorophores by using a laser like a flashlight, the emitted fluorescence light from the whole cell would mix and ultimately not allow for a precise localisation of the surface attached to the cover slip. Yet for the study on the scale of membrane constituents only the surface of the cell attached to the cover slip is of interest, not the whole cell. One way to restrict the fluorescence to a thin layer, is to only excite a thin layer in the first place.

1.3 Total Internal Reflection

To restrict the excitation to a thin layer of the specimen, usually less than 200 nanometers, total internal reflection fluorescence (TIRF) microscopy can be used. As the name suggests TIRF makes use of the fact that radiation with an incident angle greater than the critical angle of the border between two media is totally reflected (based on Snell's law of refraction). Yet due to the quantum mechanical nature of electromagnetic radiation, a tiny part of the energy passes into the other medium, with its intensity perpendicular to the border decreasing exponentially with distance to it. This leads to a *evanescent field* or *evanescent wave*, with a depth of a few 100 nm for visible light. TIRF microscopy uses this by shining a laser onto the cover slip at a supercritical angle, and so solely excites the few hundred nanometers of the cell wall attached to the cover slip. TIRF

results in a thin slice of the three dimensional specimen, which may either be treated as flat surface by 2d localisation, or as a thin 3d space by appropriate 3d localisation techniques.

1.4 Single Molecule Localisation

In order to prevent two neighbouring fluorophores to overlap, which prohibits distinction and so ultimately limits the obtainable resolution; the basic principle of direct stochastic optical reconstruction microscopy (dSTORM) and many other SMLM techniques is to separate the signal of neighbouring individual emitters in *time*, which allows to determine their positions with a precision only limited by its intensity:

$$\Delta x = \frac{\Delta k}{\sqrt{n}} \quad (1.4)$$

where Δx is the localisation precision, Δk is the full width half maximum (FWHM) of the point spread function (PSF) and n is the intensity as number of collected photons.

First, all fluorophores are put to their triplet state with intense laser light of appropriate frequency depending on the fluorophore used. In our experimental setup this means the live image gets visibly darker the more fluorophores reside in the triplet state, until dark enough to start the recording (usually a few seconds).

Now that most fluorophores reside in their dark state, upon laser activation with typically 405 nm, only the very few residing others switch to their *on* state. They repeatedly emit light by alternating between singlet state S_1 and ground state S_0 as described in section 1.1. For some fractures of a second this results in fluorophore *blinking*, until they fall back into their *off* states. This somewhat static image is recorded, much like a snapshot of the night sky with a shutter speed of 1/50 s.

This process has to be repeated many times, until all the fluorophores have been *on* several times stochastically. In our case this yields 50000 frames, each consisting of many, but mostly not neighbouring emitters.

1.5 Two Dimensional SMLM

For obtaining 2d localisations, it is convenient and most often precise enough to fit a GAUSSIAN to each of the diffuse dots in the frame, in order to estimate their centre—thus, the position of the fluorophore in sub-pixel resolution. For this thesis we used the ImageJ plugin *ThunderSTORM* [Ovesný et al., 2014] for this task.

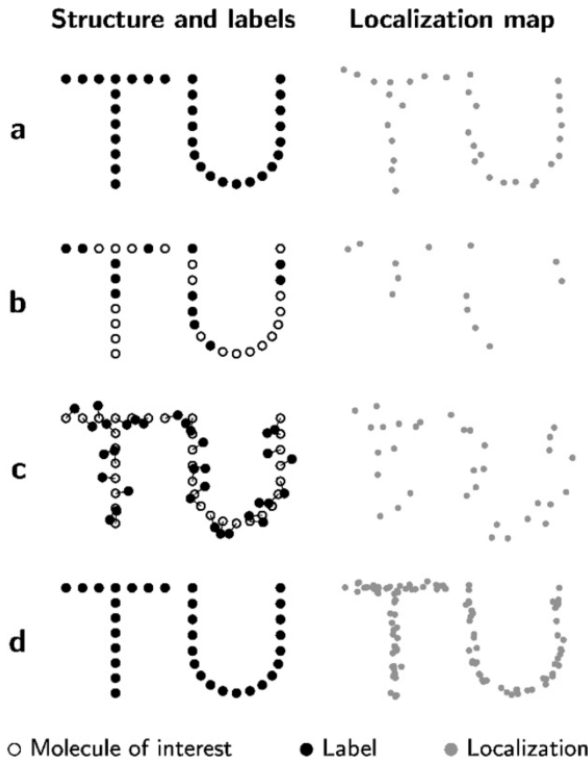


Figure 1.2: Influence of imaging parameters on the reconstructed SMLM image. The actual localization (left column) of the protein molecules (circles) yielding the obtained localization (right column), [SMLM, 2021].

In Figure 1.2, a summary of the principle of 2d SMLM is shown, including the common pitfalls: Due to localization errors, the localizations are slightly displaced from the true molecule positions (a). In addition, the structure is distorted or misrepresented by decreased labeling efficiency (b), label displacement (c) or over counting (d), [SMLM, 2021].

1.6 Three Dimensional SMLM

To be able to accurately estimate the three dimensional location of the fluorescent molecule, the PSF must be known quite well. Simply put: If one knows the shape of a point source in varying degrees of defocus, one can guess the defocus and thus the z coordinate of the fluorescence molecule.

Fitting a full point spread function (PSF)—using prior calculated ZERNIKE Modes—to such a stack of images containing reasonably spaced fluorescence signals even yields a list of 3d localisations, as explained in detail in ??.

Chapter 2

Methods

2.1 Maximum Likelihood

For the Analysis of dSTORM fluorescence microscopy, maximum likelihood estimation (MLE) is widely accepted as a gold standard; We closely follow the method from [Zelger et al., 2018] here.

First we assume the amount of photons n_k detected in pixel k can be described by a POISSONIAN probability distribution:

$$P_k(n_k|\mu_{\theta,k}) = e^{-\mu_{\theta,k}} \frac{\mu_{\theta,k}^{n_k}}{n_k!} \quad (2.1)$$

where the expectation values $\mu_{\theta,k}$ is defined as:

$$\mu_{\theta,k} = \beta + s * h_k(x_0, y_0, z_0) \quad (2.2)$$

depending on the form of the PSF model h and on the parameter vector θ :

$$\theta = (\beta, s, x_0, y_0, z_0) \quad (2.3)$$

with β and s denoting the mean photon numbers for background level respective signal; and x_0, y_0, z_0 denote the particle position in 3d.

For each recorded frame, the parameter vector θ is estimated by finding a minimum of the total negative log-likelihood function using the MATLAB tool `fminunc`:

$$\theta = \arg \min_{\theta} \sum_k \mu_{\theta,k} - n_k \ln \mu_{\theta,k} \quad (2.4)$$

2.2 PSF Model & Zernike

In first order approximation the PSF can be aberration-free, but for SMLM this is not going to be precise enough. In this thesis we employ a PSF model expressed in a ZERNIKE modes basis using NOLL coefficients ranging from 2 to 37 (3rd order spherical aberrations) plus the 4th order spherical mode Z_{56} [Zelger et al., 2018]:

$$\Phi = a_{56} Z_{56} + \sum_{i=1}^{37} a_i Z_i \quad (2.5)$$

2.3 STORM & dSTORM

We used dSTORM microscopy throughout this thesis, which is the *direct* variant of STORM, utilising very bright fluorophores, with a high rate of photoswitching and minimal photo-bleaching, based on [Heilemann et al., 2008].

2.3.1 Gloxy Buffer

The principle of stochastic optical reconstruction microscopy (STORM) on cells is based on an appropriate *storm buffer*, which suppresses the activation of the *bright state*, and limits the amount of oxygen, the main source of photo-bleaching.

Single color SMLM at 645 nm (red) employs the Gloxy buffer, so called after its central ingredients glucose and glucose oxidase. We used

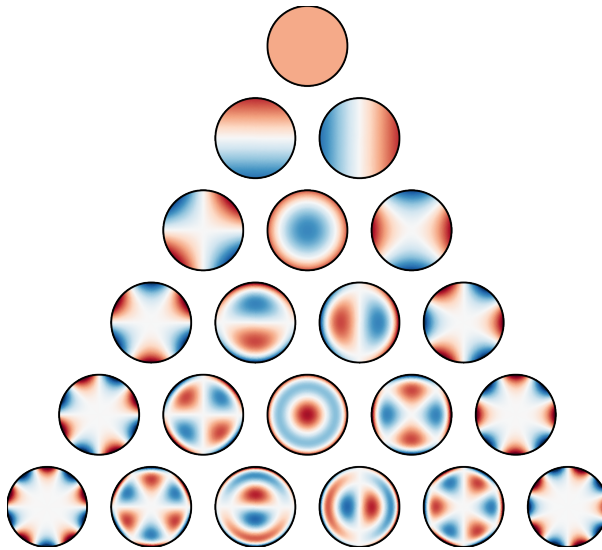


Figure 2.1: The first 21 Zernike polynomials, ordered vertically by radial degree and horizontally by azimuthal degree, obtained under CC-BY-SA license from [Nschloe, 2023].

throughout this paper for all single channel measurements at 645 nm unless noted otherwise.

Gloxy buffer concentration

- 50 mmol β -mercaptopropylamine hydrochloride (MEA) (Sigma-Aldrich).
- 10 vol% of a 250 g L^{-1} solution of glucose.
- 0.5 mg mL^{-1} glucose oxidase.
- 40 mg mL^{-1} catalase (Sigma-Aldrich).
- with phosphate-buffered saline (PBS) adjust to pH 7.6 .

2.3.2 OxEA Buffer

Dual colour fluorescence microscopy poses novel challenges to find a proper dSTORM buffer, that simultaneously works for two distinct fluorophores AF647 and AF488—thus

both excitation wavelengths—without interfering with each other. The buffer composition we used is based on [Nahidazar et al., 2016], and called OxEA after its main ingredients OxyFlour and MEA:

OxEA buffer concentration

- 50 mmol MEA (Sigma-Aldrich).
- 3 vol% OxyFlourTM (Oxylase Inc., Mansfield, Ohio, U.S.A.).
- 20 vol% of sodium DL-lactate, 60% syrup (L1375, Sigma-Aldrich).
- with PBS adjust to pH 8–8.5 with NaOH.

2.4 Dual Colour Optics

It is possible to use different excitations to simultaneously measure different fluorescence markers, but for that the point spread function has to be known for each wavelength. So the PSFs are estimated both for red and blue laser light, with the phase retrieval program by [Zelger et al., 2018]. As a sort of *ground truth* due to their well known geometry, 100 nm beads stained with fluorescence dyes are used. For both red (645 nm) and blue (488 nm) laser light, a stack of 50 dSTORM images is taken; each at focal depths (from -1600 nm to 1600 nm in 200 nm steps). the 17 stacks are averaged, and fed into the phase retrieval program as a **tiff** file, to estimate the wavelength specific PSF.

2.4.1 Aberration Correction Collar

To further complicate things, the new 1.5 NA Olympus objective comes with a correction collar to compensate for aberrations—which naturally vary slightly for both colour channels. In order to find the best correction collar setting of the Olympus 1.5 NA objective for SMLM,

the point spread functions (PSF) is computed for each of the three settings of the correction collar $\{0.13, 0.17, 0.19\}$; using the program by [Zelger et al., 2018], described in Section 2.2.

2.4.2 Cramér Rao Lower Bound

The CRAMÉR RAO lower bound (CRLB) gives the theoretical limit for the localization precision (with any unbiased estimator). A detailed description would exceed the scope of this paper, the interested reader is referred to a rather recent tutorial [Chao et al., 2016].

In order to find the best correction collar setting of the Olympus 1.5 NA objective for SMLM, the CRLB is computed using the MATLAB program `crlb.m`, with prior estimated PSF via phase retrieval [Zelger et al., 2018].

The CRLBs for parameter uncertainties are given by the corresponding diagonal elements in the inverse FISHER information matrix \mathbf{F} , which is calculated as follows [Chao et al., 2016]:

$$\mathbf{F}_{m,n} = \sum_k \frac{1}{\mu_{\theta,k}} \frac{\Delta\mu_{\theta,k}}{\Delta\theta_m} \frac{\Delta\mu_{\theta,k}}{\Delta\theta_n} \quad (2.6)$$

All CRLBs are computed at a defocus position of -500 nm, in steps of 5 nm from 0 to 500 nm. For all Estimations we assume identical, arbitrary yet consistent signal strength (2500) respective background (100).

2.5 Dual Colour Projection

Since we measure excitation with different lasers on the same channel, we propose alternating the sets to ensure the comparability of the two sets of images; so that they are affected by drift over time, bleaching, etc. in the same way.

The generated image stacks are then split and fed separately through the SMLM algorithm, since the PSF model depends on the emitted wavelength—and thus on the excitation. The two obtained data sets with localisations for both channels are then analysed together.

Since the methods used to obtain 3d SMLM data are wavelength dependent, the two channels will most likely be *off*, yet we ultimately want to overlay them. We hereby propose a calibration step, based on evaluating evenly dyed beads in both channels, analysing the localisations, and finally figuring out their offset.

2.5.1 Rigid Transform

In first order approximation, this offset may be thought as linear, so the two sets are related via a *rigid transform*; thus only by rotation and translation. Such a transformation can be solved easily via linear algebra; the solution used here is one of the many known ways, using least squares and singular value decomposition (SVD) based on [Arun et al., 1987].

In this short overview, the lines refer to the function `rig()` shown in Section A.3.3, where the full code is listed. Basically, one first calculates the centroids of the two sets of points p, q , and shifts both sets to their respective centres, thus eliminating translation (block 1 at Lines 24–28). As a second step the *best* (least squares) transform that *rotates* the set p to the set q is found via SVD (block 2 at Lines 30–51). As a last step the translation between set p and q is computed using the known rotation (block 3 at line 53).

2.5.2 Affine Transform

The next more complex approach includes other—nonlinear—transformations like *shearing* or *scaling*, called an *affine transform*. Our approach is based on [Qu et al., 2010], and can

be viewed as a more complex variant of the rigid transform shown in Section 2.5.1, still using least squares and singular value decomposition (SVD) to find the optimal affine transform in three dimensional euclidean space, based on [Arun et al., 1987].

Between centering and SVD, which both follow the rigid transform, a *orthogonal reduction* is performed (block 2 at Lines 37–60). Here the covariance matrices of both sets \mathbf{p} and \mathbf{q} are computed, to form their inverse via a CHOLESKI decomposition (Lines 44–49). The already centred sets \mathbf{p} and \mathbf{q} are subsequently orthogonalised (Lines 51–56); so that \mathbf{p} and \mathbf{q} are now solely related by a rotational matrix.

2.5.3 Simulation

As a proof of concept, we performed both a rigid and an affine recovery on simulated data. The code for this simulations is listed in Section A.3.6, as well as in the Octave program `simulate.m` at my Git repository at [Siegel, 2021]. First, each simulation creates a cylinder-shaped pseudo-random point cloud \mathbf{p} , and deducts some projection to get a second set \mathbf{q} , related to \mathbf{p} by either a rigid or an affine transformation.

2.5.4 Projected 2d NPC

As a second proof of work, we tested both rigid and affine recovery on several real dual colour SMLM data sets of labeled nuclear pore complex (NPC)s of two-colour in-focus measurements of different cells, successively recorded within the same sample. The fluorescence images are analysed with *ThunderSTORM* [Ovesný et al., 2014], a dSTORM plugin for *ImageJ*, to obtain 2d localisations based on GAUSSIAN fits.

Since these data sets are two dimensional, we added low-magnitude noise ($\mathcal{O}(10^{-3})$) as a virtual z component, so both sets are pro-

jected almost onto the z plane for analysis. This is necessary, because the singular-value-decomposition faults on 2d data.

The resulting data sets are then analysed either a rigid or an affine transformation.

This process is centrally governed by the Octave program `cockpit.m`, which internally uses the Octave function `ampel.m` to sort the imported data file into the two alternating colour channels. The code is listed in Section A.3.1, and Section A.3.2, as well as in my Git repository at [Siegel, 2021].

Cockpit

To begin with, the Octave program `cockpit.m` acts as a framework for the entire analysis; successively loading the content of all lokal 2d location files (unless specifically excluded using the `exclude` variable). All parameters for further analysis are confined to the settings block at the beginning, e.g. load-order corrections due to frames being skipped, etc.

Sort

The function `ampel.m` sorts (modulo) the positions in three categories—red, blue, empty—based on the frame, in which the respective positions have been found by prior localisation. The illumination order (e.g. red-blue-empty) has to stay constant, but the offset (which one of the three staging the starting frame) can, and unfortunately currently has to be adjusted for each file manually by specifying mod values.

Cluster

The three separate channels red/blue/empty are then clustered by `dbscan.m`, based on two parameters: euclidean distance between two neighbours (`eps`), and least number of points required to be considered a cluster at all (`minpts`). Based on these parameters, some ensemble of dots are considered a cluster while

others are not, which is the whole point of these routines. Naturally, the number of clusters vary with different data sets. Unfortunately though, a rigid projection demands sets of the same size. Brief parameter tuning reveals: Whatever parameters, some regions most likely will have to be excluded.

Chapter 3

Results

3.1 Dual Colour Buffer

Beads

The beads (polystyrene spheres) we use for calibration of the phase retrieval algorithm are soaked in *Alexa Fluors* AF647 respective AF488 and imaged in pure water.

Living cells like our prepared NPC samples are labeled with both *Alexa Fluors* AF647 and AF488 in glucose oxidase dSTORM buffer (Gloxy) buffer, described in detail in Section 2.3.1.

Gloxy is designed for Alexa Fluor AF647 and works with it as expected. The buffer failed for AF488 excitation with appropriate light: The recorded intensity quickly degraded due to bleaching to about an order of magnitude lower than for AF647.

In order to enable similarly precise dual colour three dimensional SMLM, by using alternating excitation with red and blue laser light the buffer constituents were found to play a central role.

OxEA buffer protocol

Finally the NPC samples have been evaluated using OxyFlour β -mercaptoethylamine hydrochloride dSTORM buffer (OxEA) buffer, described in detail in Section 2.3.2. OxEA was found to work well with either red or blue ex-

citation.

For about 1 mL of OxEA buffer we used the amounts shown in Table 3.1, to obtain above listed concentrations.

Table 3.1: Ingredients used for preparation of OxEA buffer for dual colour dSTORM.

Order	Ingredient	Store	Vol / μL
1	Ultra pure H_2O		600
2	10 M NaOH		20
3	10× PBS		100
4	60% DL-lactate	fridge	200
5	1 M MEA	freezer	50
6	OxyFluor	freezer	30

The OxEA buffer did work, but offered notably less fluorophore blinking, as well as was much lower SNR for the red channel compared to using Gloxy buffer; with the blue channel being worse still.

Nevertheless OxEA clearly beat Gloxy in being able to buffer both AF647 and AF488 simultaneously, thus was used in all further measurements.

pH

The pH of the OxEA buffer is checked using both broad range pH testing strips, and a dig-

ital pH meter, to be between pH 7 and pH 8.

3.2 Dual Colour Optics

3.2.1 Zernike Modes

The calculated ZERNIKE modes of the PSF are shown for each of the three correction collar settings $\{0.13, 0.17, 0.19\}$, each for blue channel respective red channel in Figure 3.1 respectively Figure 3.2.

For convenience the same results are additionally shown grouped by the the three correction collar settings $\{0.13, 0.17, 0.19\}$, now for both red and blue channel in Figure 3.3, Figure 3.4 and Figure 3.5.

The aim is now to find a correction collar setting where the ZERNIKE modes are both low and similar for red and blue excitation.

As an overview the various settings lead to distinguishable ZERNIKE modes, yet in a similar order of magnitude (from 0 to about 0.1 au), as can be seen in all the mentioned figures.

As an example: In Figure 3.4 showing setting of 0.17, one can see that there is a huge difference in ZERNIKE mode number 22; red light at 0.01, where blue light gives 0.06.

We can also clearly see that for the setting of 0.13 the aberrations for red mostly exceed those of blue light, indicating that this might not be a good choice ZERNIKE mode wise.

On the other hand we can see that while equal for red and blue the ZERNIKE modes for setting 0.19 features high lower orders, which even if evenly for both colors is not desirable.

A closer inspection suggests that at setting 0.19 the magnitude of the calculated ZERNIKE modes is quite similar to the one with setting 0.17, yet slightly higher in all respects; which supports ruling out the correction color setting 0.19.

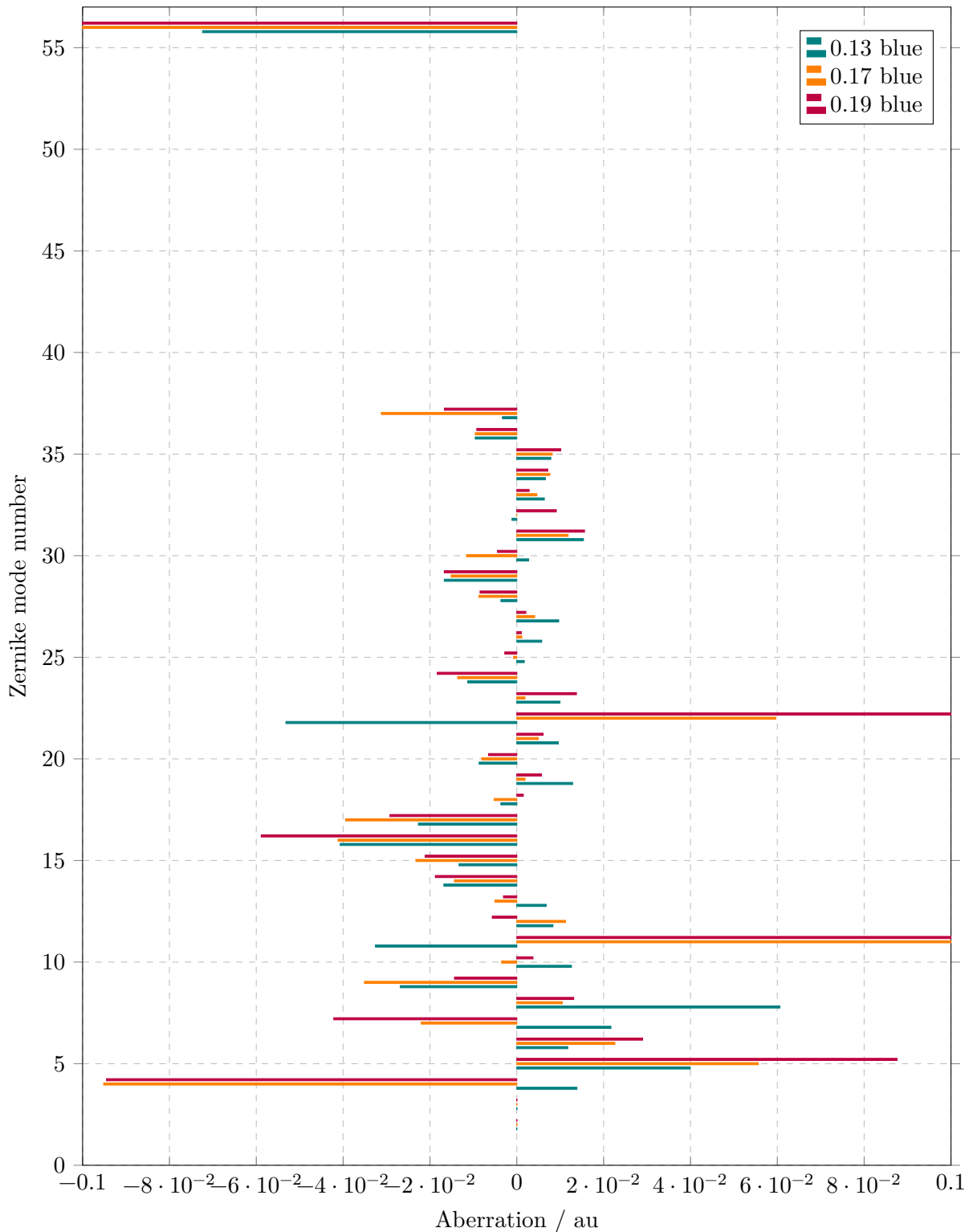


Figure 3.1: Blue channel ZERNIKE modes {1 ... 37,56} versus aberrations of PSF model via phase retrieval, for all three correction collar settings (0.13, 0.17, 0.19).

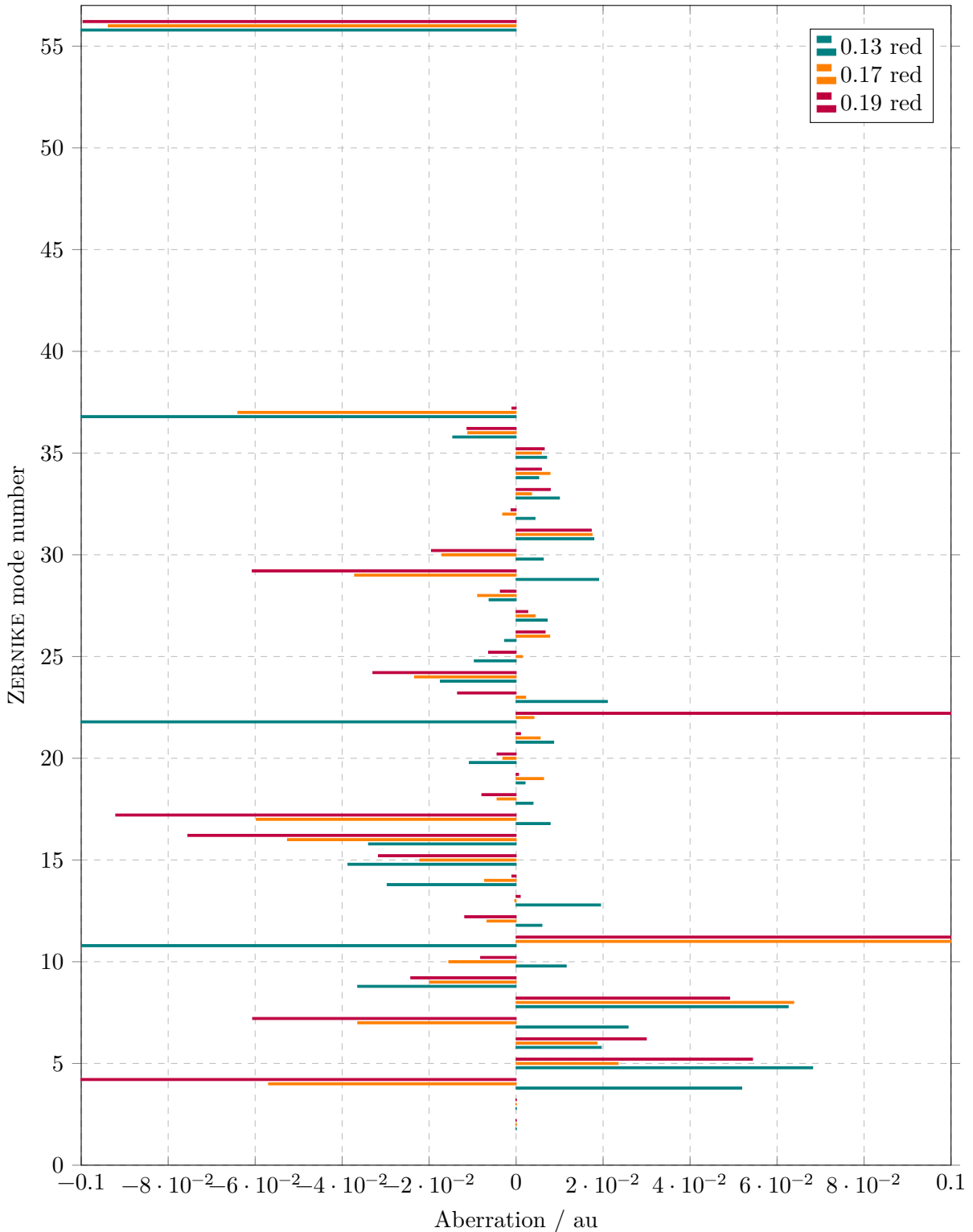


Figure 3.2: Red channel ZERNIKE modes {1 ... 37, 56} versus aberrations of PSF model via phase retrieval, for all three correction collar settings (0.13, 0.17, 0.19).

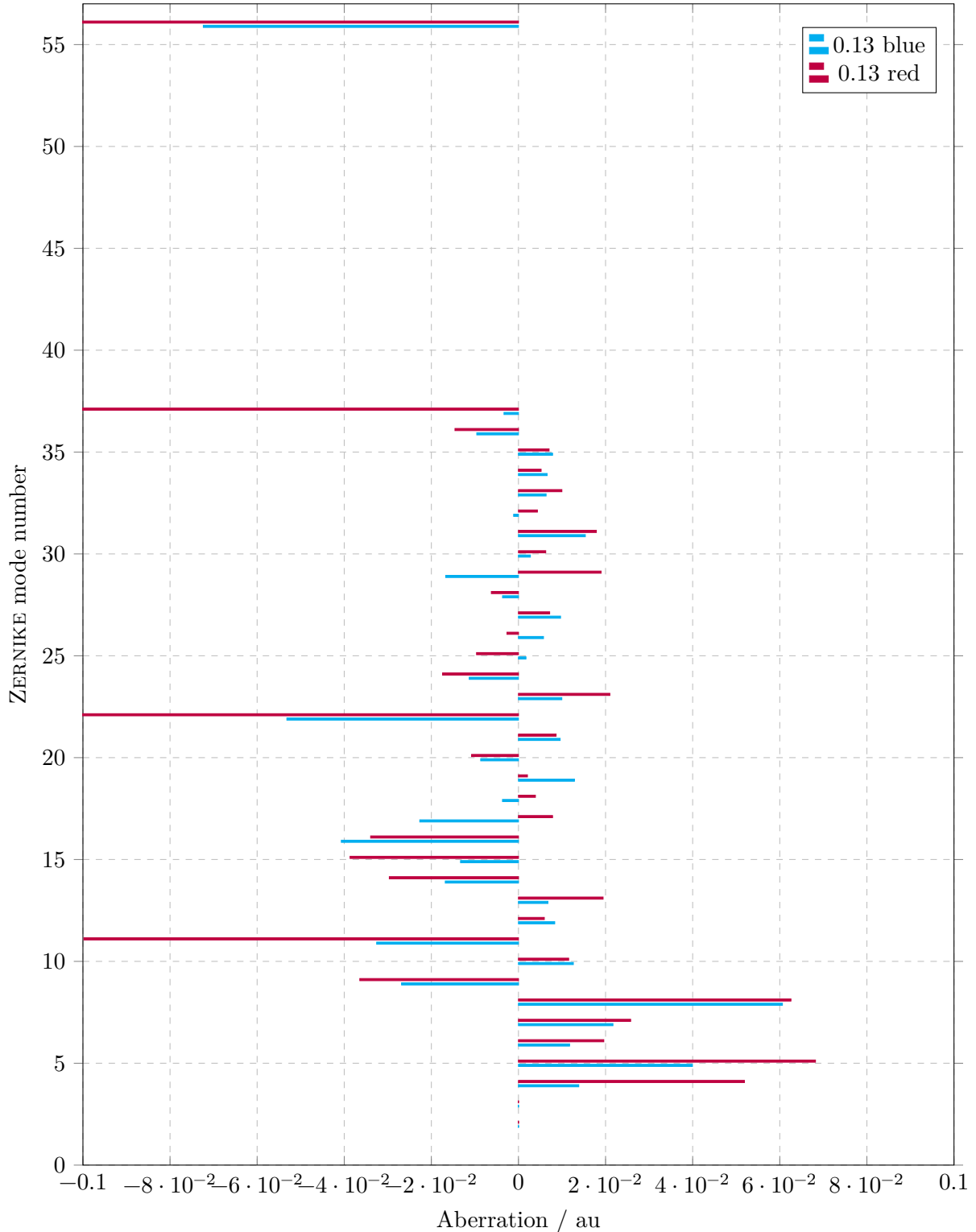


Figure 3.3: Red and blue channel ZERNIKE modes {1 ... 37, 56} versus aberrations of PSF model via phase retrieval, for correction collar setting of 0.13.

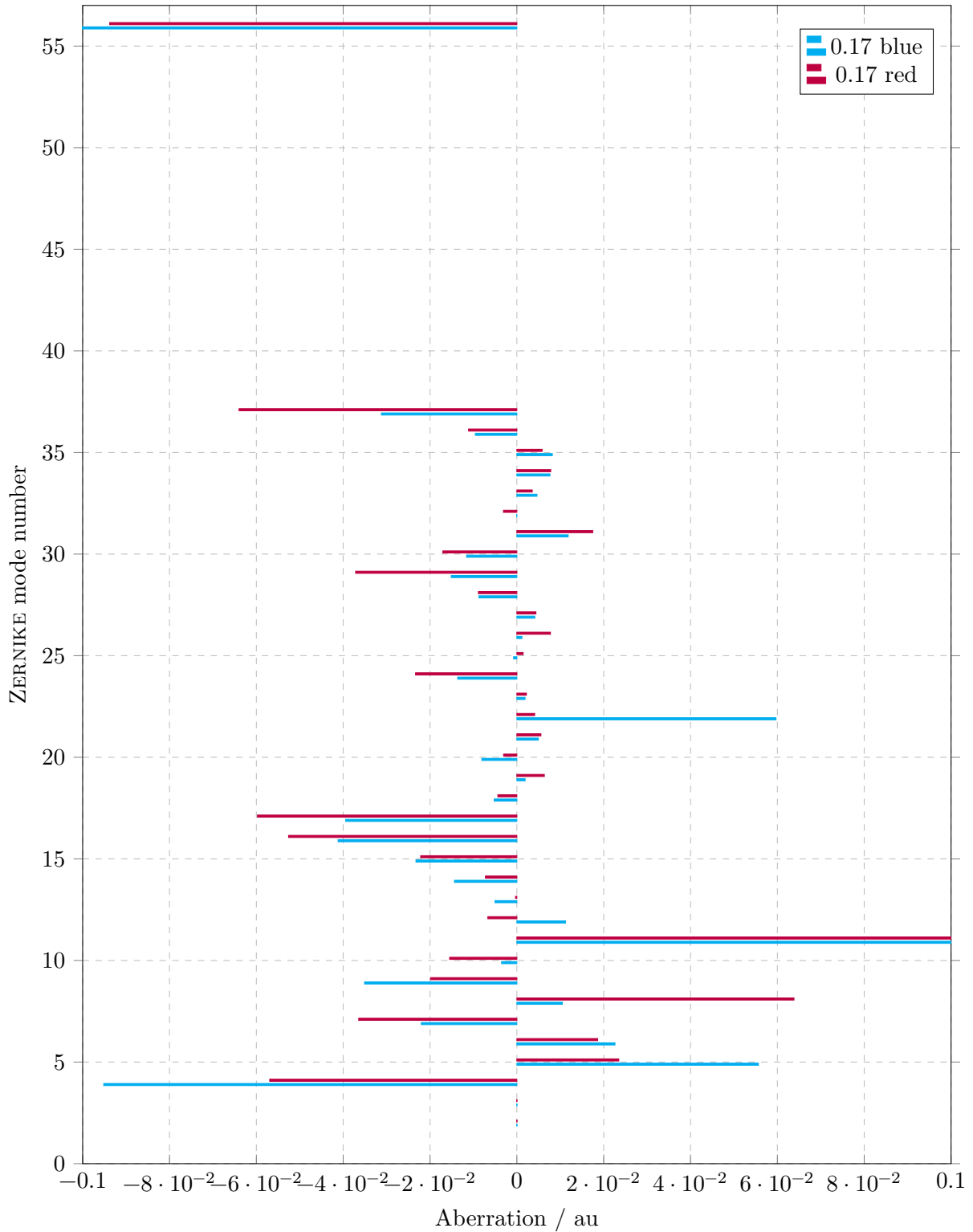


Figure 3.4: Red and blue channel ZERNIKE modes {1 ... 37, 56} versus aberrations of PSF model via phase retrieval, for correction collar setting of 0.17.

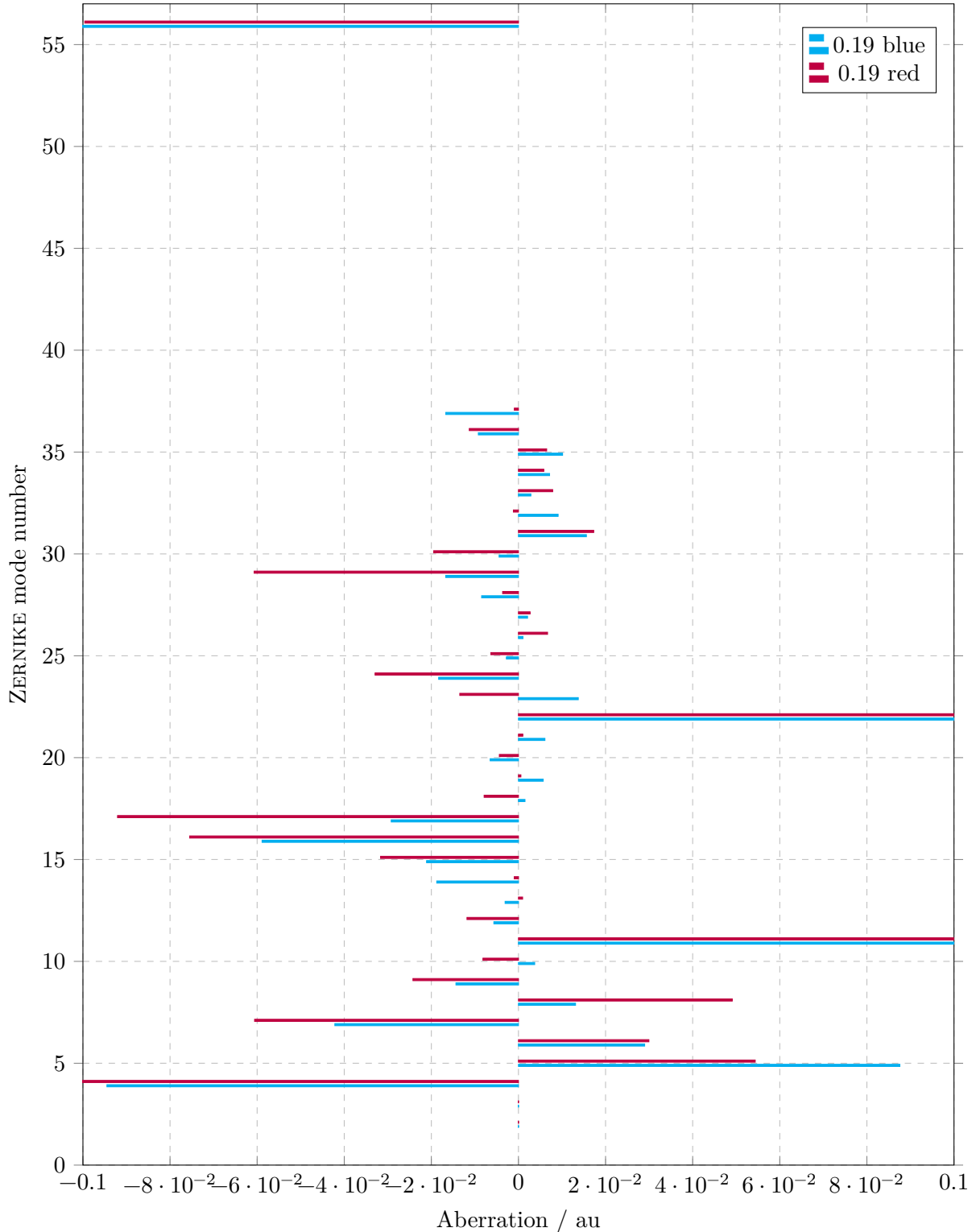


Figure 3.5: Red and blue channel ZERNIKE modes {1 ... 37, 56} versus aberrations of PSF model via phase retrieval, for correction collar setting of 0.19.

3.2.2 Cramér Rao Lower Bound

The Estimated CRAMÉR RAO lower bound (CRLB) are calculated for different correction collar settings as shown in section 2.4.2 using the ZERNIKE modes described in section 3.2.1.

All results are shown together in Figure 3.6; the different correction collar settings (varying linestyles for 0.13, 0.17, 0.19) of the Olympus 1.5 NA objective; for X , Y and Z axis (top, middle, and bottom); for both red and blue channel (colours).

Additionally plots grouped by X , Y and Z axis are shown in Figure 3.9 for red light and Figure 3.7 for blue light. Finally plots grouped by different correction collar settings are shown in Figure 3.10 respective Figure 3.8.

The CRLB presents an estimation of the obtainable resolution both lateral (X , Y) as well as depth (Z).

Obviously the various correction collar settings lead to different obtainable resolution. For SMLM we are interested in defocusing some 200 nm, so we want the lowest possible X , Y and Z CRLB values, ideally for both red and blue.

From 3.6 it can be seen that the CRLB values are roughly the same for red and blue light. So we only need to select the correction collar with the best overall resolution, thus the lowest CRLB values. An inspection of Figure 3.10 hints to the exclusion of the 0.19 setting, as the depth (Z) CRLB is quite high in the range between 0 and 250 nm.

On the one hand both the X and Y CRLB values for correction collar setting 0.19 and 0.17 are lower than 0.13 in the range between 0 and 250 nm. On the other hand the depth resolution Z CRLB values for 0.19 and 0.17 are much higher than for 0.13.

Considering both the lateral (X , Y) as well as depth (Z) resolution, we might consider 0.13 or 0.17 both offer a good compromise. 0.13 features better depth while worse lateral resolution, and 0.17 vica versa.

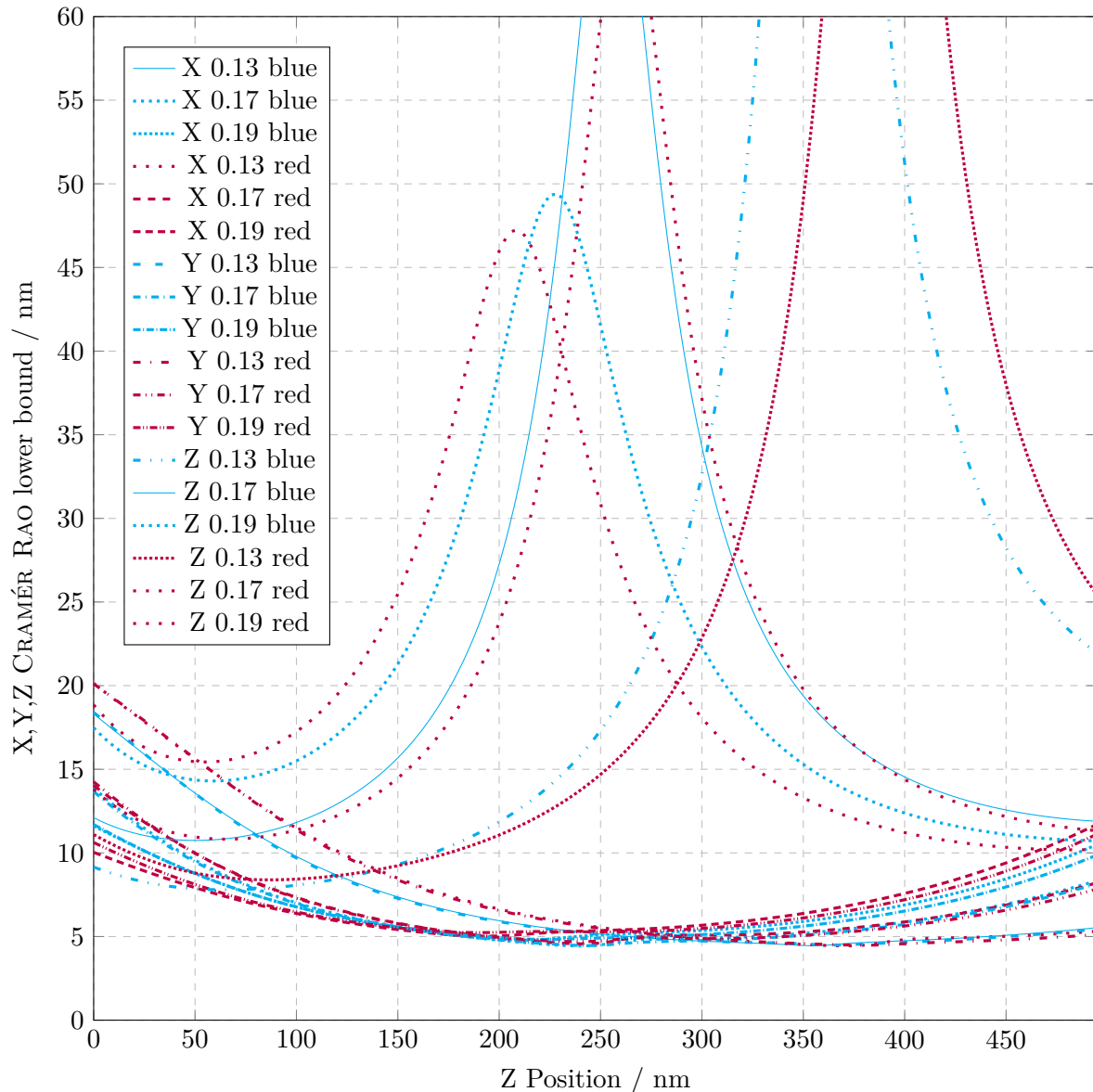


Figure 3.6: Estimated CRAMÉR RAO lower bound for different correction Collar settings (varying linestyles for 0.13, 0.17, 0.19) of the Olympus 1.5 NA objective; for X, Y and Z axis (top, middle, and bottom); for both red and blue channel (colours).

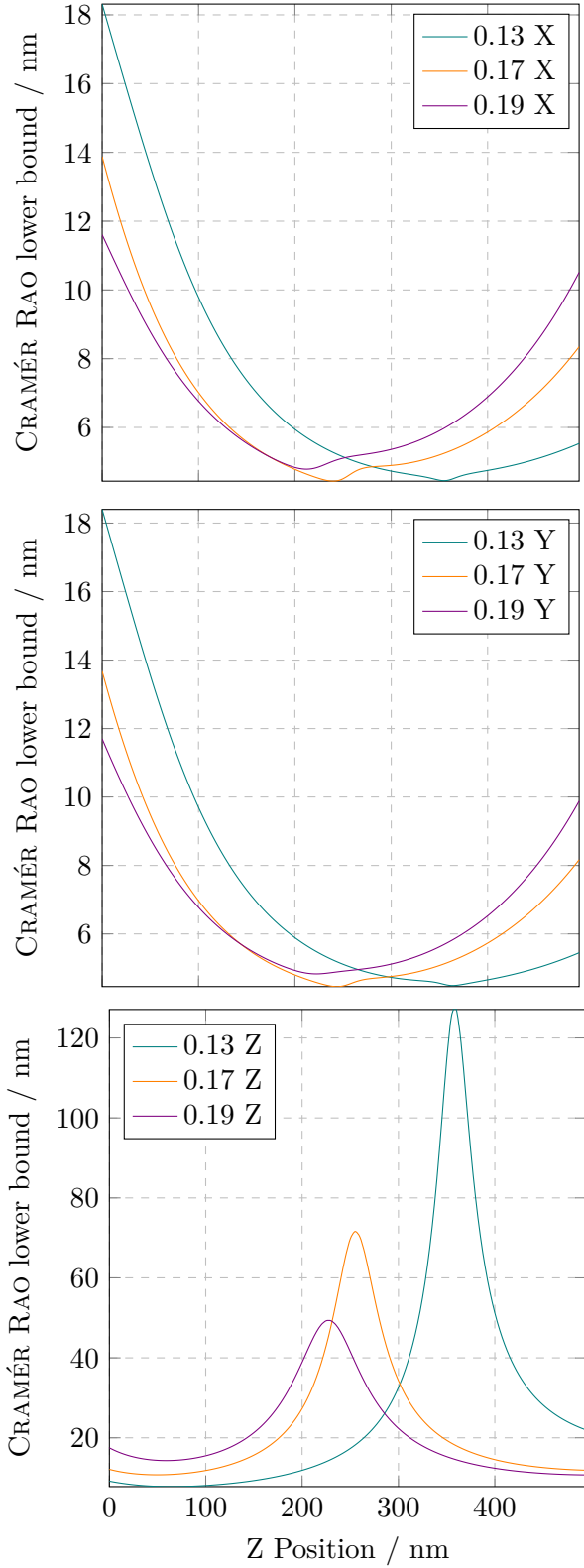


Figure 3.7: Estimated CRAMÉR RAO lower bound for blue light for different correction Collar settings (teal: 0.13, orange: 0.17, purple: 0.19) of the Olympus 1.5 NA objective; grouped by X, Y and Z axis (top, middle, and bottom).

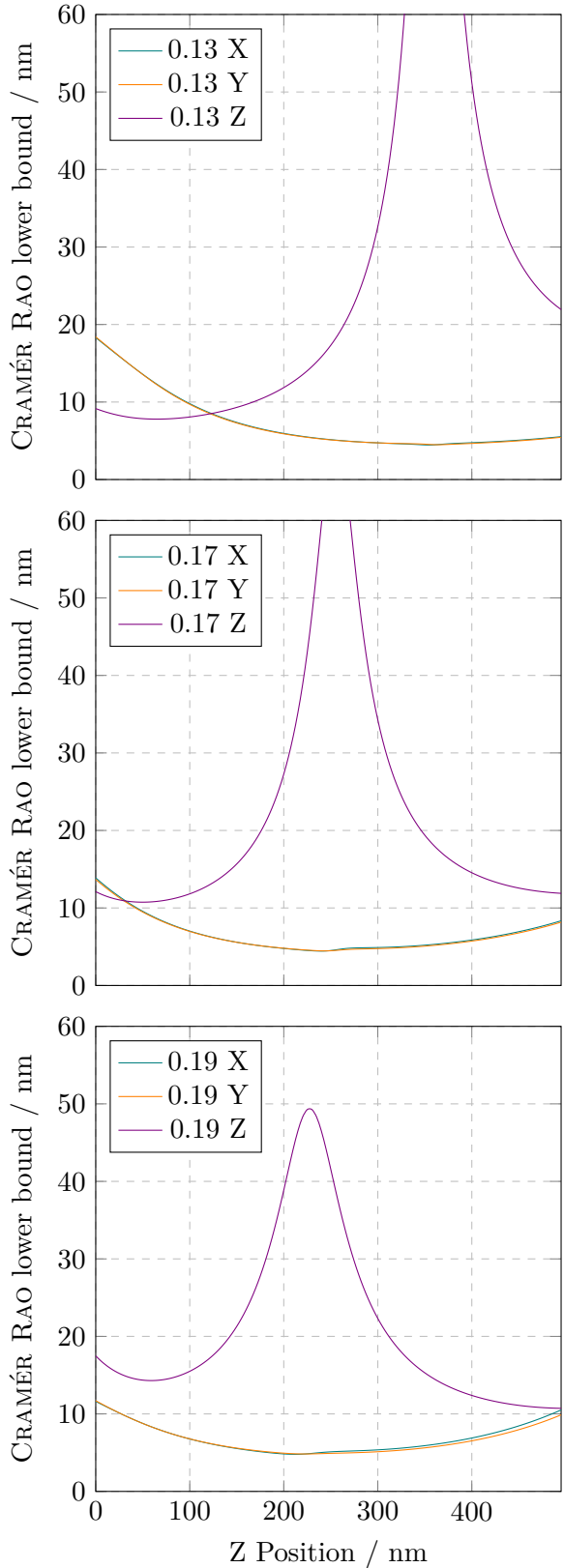


Figure 3.8: Estimated CRAMÉR RAO lower bound for blue light for X, Y and Z axis (teal, orange and purple lines); grouped by different correction Collar settings (top: 0.13, middle: 0.17, bottom: 0.19) of the Olympus 1.5 NA objective.

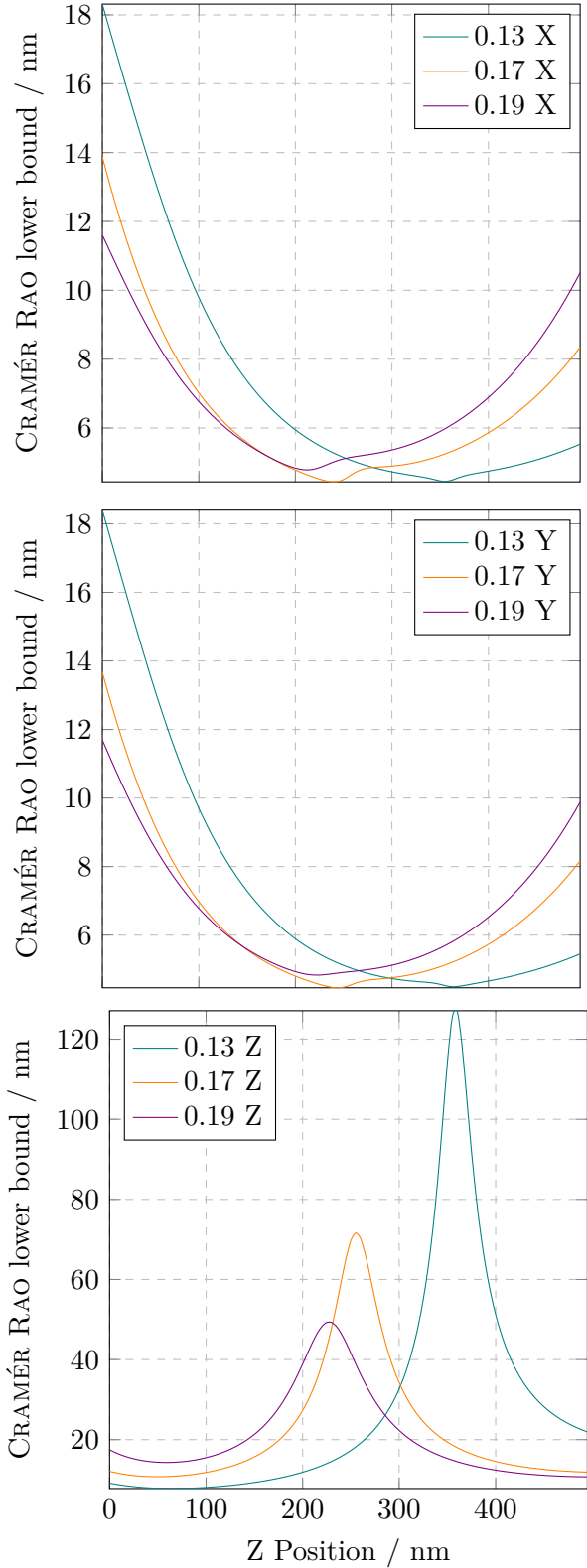


Figure 3.9: Estimated CRAMÉR RAO lower bound for red light for different correction Collar settings (teal: 0.13, orange: 0.17, purple: 0.19) of the Olympus 1.5 NA objective; grouped by X, Y and Z axis (top, middle, and bottom).

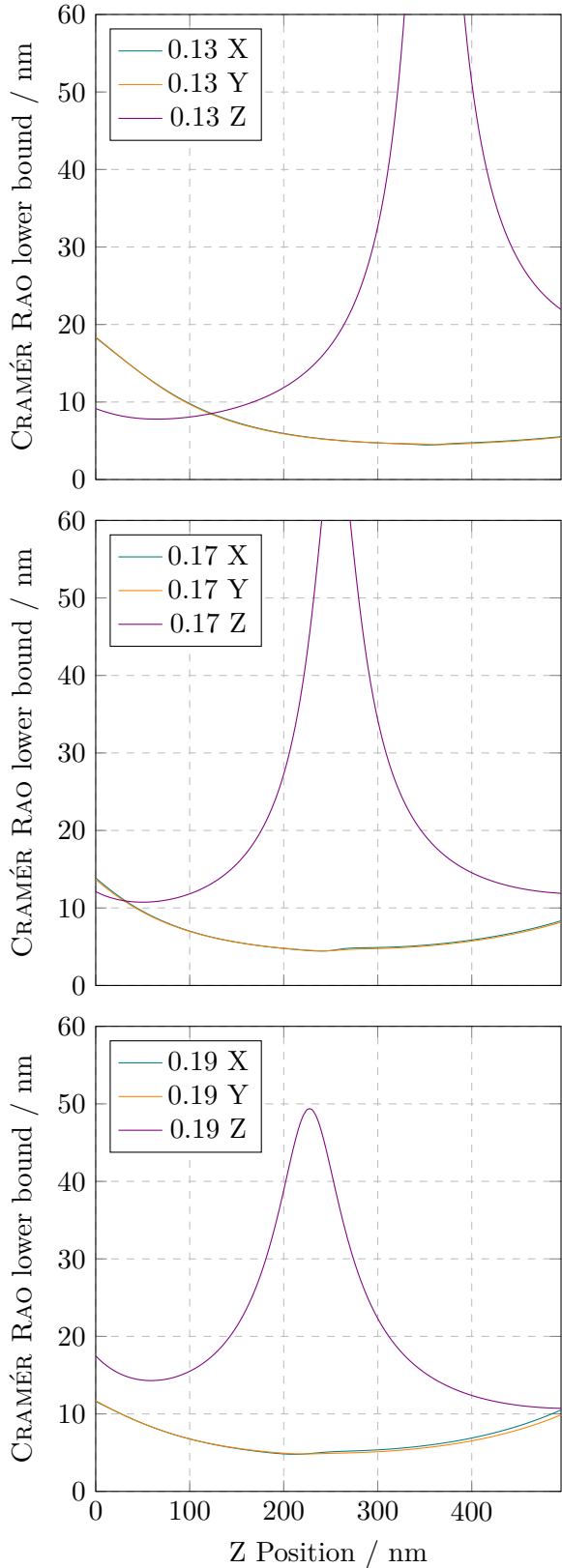


Figure 3.10: Estimated CRAMÉR RAO lower bound for red light for X, Y and Z axis (teal, orange and purple lines); grouped by different correction Collar settings (top: 0.13, middle: 0.17, bottom: 0.19) of the Olympus 1.5 NA objective.

3.3 Two Dimensional SMLM

In-focus, one colour, two dimensional SMLM is performed on all the samples, and evaluated by *ThunderSTORM* via *ImageJ*. This gives a good x,y precision; an ideal reference for the later three dimensional localisation, whose x,y precision will most likely be much lower.

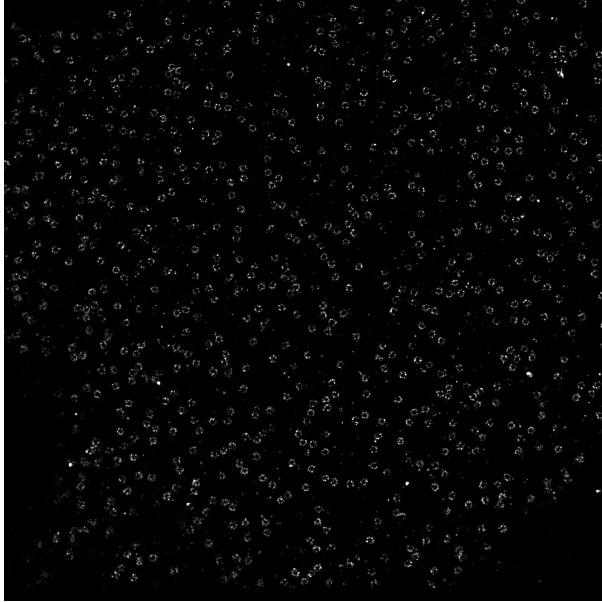


Figure 3.11: Example overview of a set of two dimensional SMLM data of NPCs, the labeled NPC tori are clearly visible.

Figure 3.11 and Figure 3.12 show an example overview (respective zoom) of a set of two dimensional SMLM data of NPCs using dSTORM with Gloxy buffer. The labeled NPC tori are clearly visible, even the more or less eight-fold symmetry of the nucleoporins is resolved.

For comparison Figure 3.13 shows a reconstruction of a human NPC from [Bley et al., 2022] where the eight-fold symmetry is clearly visible.

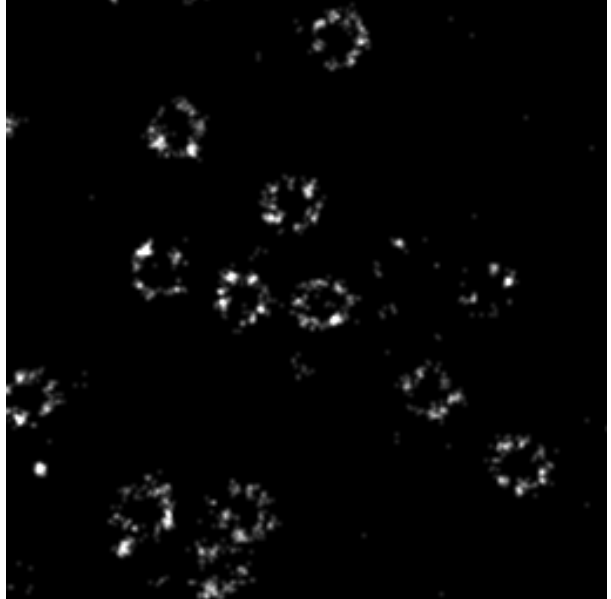


Figure 3.12: Zoom of Figure 3.11, Example of a set of two dimensional SMLM data of NPCs; The labeled NPC tori are clearly visible, even the more or less eight-fold symmetry of the nucleoporins is resolved.

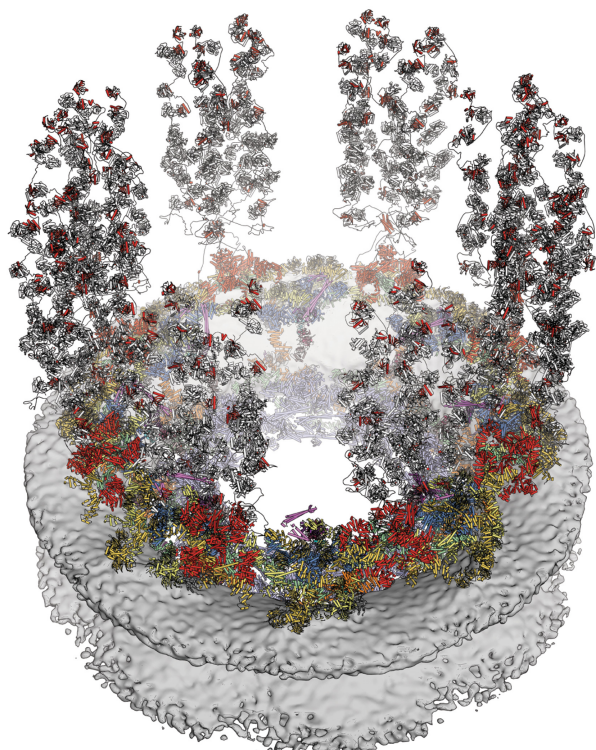


Figure 3.13: Cytoplasmic face of the human NPC. Near-atomic composite structure of the NPC generated by docking high-resolution crystal structures into a cryo-ET reconstruction of an intact human NPC. The symmetric core, embedded in the nuclear envelope, is decorated with NUP358 (red) domains bound to Ran (gray), flexibly projected into the cytoplasm, and CFNCs (pink) overlooking the central transport channel. Figure and description from [Bley et al., 2022].

3.4 Three Dimensional SMLM

Defocused, one colour, three dimensional SMLM is performed on some of the samples, and evaluated as described in Section 2.1. From the stack of 50k microscopy images, one obtains a list of localisations comprised of position (x, y, z), photon count (n), and a fit parameter (fit). Where the sans serif typeset letters refer to the variables in the code listed in this chapter.

In this section I want to describe our data analysis pipeline, in order to cut down the massive amount of initial localisations—in our example case over 130k—to distill it to the most meaningful conclusions.

As a proof of work we used NPCs as sort of a well defined biological test target. As these are used frequently for the purpose of validating a new method, it would be nice to quickly evaluate of *how good are the NPCs resolved*. The Section 3.5 is thus dedicated to find some metric for *best resolved* NPCs.

This analysis is performed in *Python*, and is freely available in my *Git repository* [Siegel, 2021]; both as a plain *Python* file (*.py*) as well as in the format of a *Jupyter Notebook* (*.ipynb*).

A slightly shortened version of the code is also shown in Appendix A for each Subsection. For the sake of readability we omit the code sections generating the shown plots, as they are mostly redundant. Of course the full code is available online.

3.4.1 Import

Here we import the used packages and the data file we obtain from running the SMLM algorithm.

3.4.2 Drift Correction

The *drift* of the setup over time can be estimated using *ImageJ*, and is then imported as **drift**. In the following block the drift correction is applied to all the 130k localisations, shown in Figure 3.14 as 3d plot of all the initial 370k drift corrected localisations.

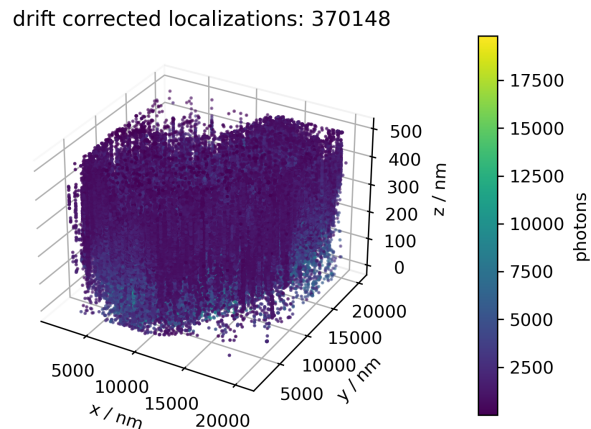


Figure 3.14: 3d plot of all 370148 drift corrected localisations, colour coded by photon count.

3.4.3 Photon Counts

As a preliminary step it might prove useful to look at the photon count statistics, shown in Figure 3.15. Here we can easily see what the supposed intensity of a single molecule is; the peak, in our case about 2000. Those localisations below may be considered noise, those far above are probably overlapping or stacked molecules, so their intensities add up.

3.4.4 Filter

In this first filter we limit the dataset to the more meaningful points; like those with intensities between 2k and 7k. Also since we defocused for 500 nm, only those **z** values between 0 and 499 can be considered realistic. Here 0

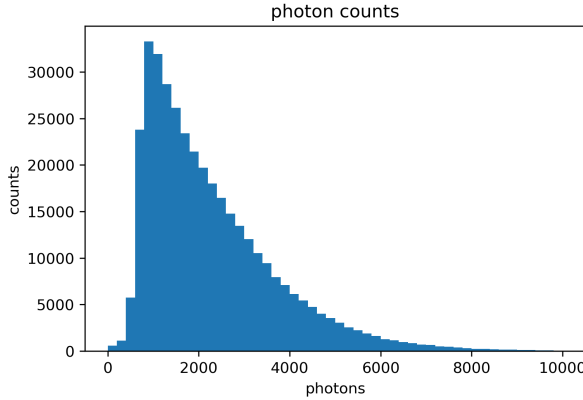


Figure 3.15: histogram of the photon count for the localisations.

means directly attached to the glass substrate, so negative values would be *inside* the glass substrate; and thus need to be discarded as unphysical. The dataset could be filtered by `min_fit`, but to our findings this does not contribute much.

Figure 3.16 shows a 3d plot of the remaining 154k localisations after we apply the filter, thus effectively shrinking down our exemplary data set by about 40%.

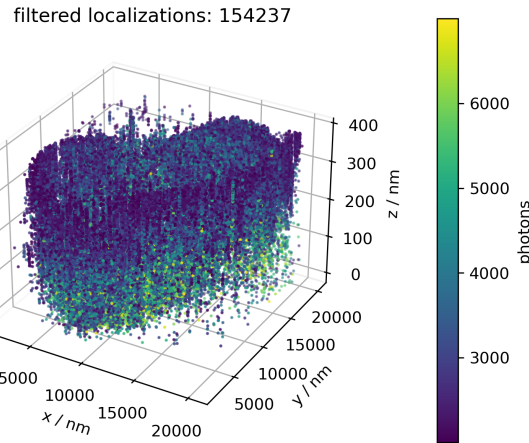


Figure 3.16: 3d plot of all 154237 filtered localisations, colour coded by photon count.

3.4.5 Track Particles

The 50k frames we analyse here are taken with exposure of 20 ms, and 10 ms between consecutive exposures. Depending on the laser intensity and the buffer composition the bright state has a specific lifetime τ . This leads to one exemplary molecule being *on* for some 30 ms (one frame) while some other is on for 60 ms; and so appears in two consecutive frames. Since the molecule in those two frames essentially is the same, we can *track* it over time: effectively averaging the location if present in multiple frames, thus reducing the amount of localisations while at the same time increasing their precision.

The parameters `sr` denotes the *search range*, how far apart two consecutive localisations are still considered *one* particle, this has to be adjusted based on the physical setup considering vibrations and the like.

Figure 3.17 shows a 3d plot of the remaining 98k localisations, after we track the particles. So the tracking step further shrinks down our exemplary data set by about 60%.

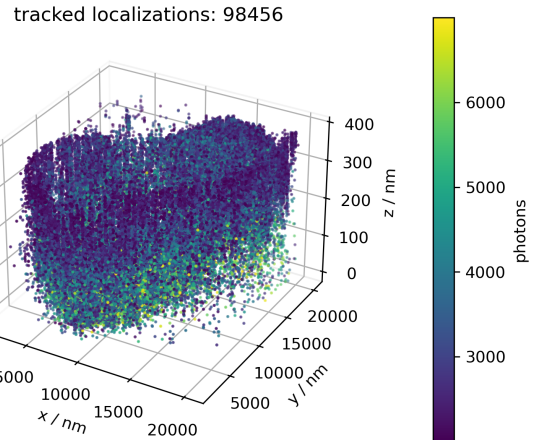


Figure 3.17: 3d plot of all 98456 filtered localisations, colour coded by photon count.

3.5 NPC Analysis

We use NPCs as a test target for our method, thus we have some additional knowledge, like the geometry of each individual NPC: they comprise two stacked tori, each about 150 nm diameter (in x,y direction), and 150 nm apart (in z direction). Mind that in Figure 3.13, the reconstruction of a human NPC from [Bley et al., 2022], only the Cytoplasmic face is shown. The protein groups forming the torus are shown in colors on the grey membrane surface. The second torus is on the core side of the nuclear envelope, and is not shown here.

Now we can group our dataset with close to 100 thousand localisations to clusters of roughly this size in x,y (set `dim=2`). Note that for the sake of completeness, we include the possibility of clustering in 3d to spheres in x,y,z (set `dim=3`), but mind that x,y and z precision most often greatly varies (see Section 3.2.2).

The parameter `min_samples` denotes the minimum amount of constituents a cluster must have to be considered such.

Figure 3.17 shows a 3d plot of the localisations of 658 identified clusters, omitting all the other 35489 localisations as noise. So the clustering step further shrinks down our exemplary data set by about 30%.

3.5.1 Clustering

Figure 3.18 shows the localisations of the 658 identified clusters (omitting 35489 localisations as noise, due to not belonging to a cluster), colour coded by photon count.

In our experiments a density based clustering algorithm `dbscan` [Ester et al., 1996] worked better than `kmeans`.

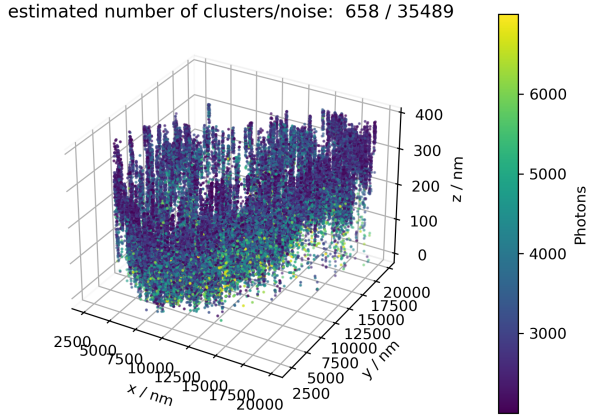


Figure 3.18: 3d plot of the localisations of the 658 identified clusters (omitting 35489 localisations as noise, due to not belonging to a cluster), colour coded by photon count.

3.5.2 Cluster Analysis

For all the localisations within each of these identified clusters, we now derive the centroid position (`xmean`, `ymean`, `zmean`), with standard deviation (`xvar`, `yvar`, `zvar`). This enables the classification of the within-cluster distribution of localisations, alas how well they represent the anticipated NPC geometry.

To obtain this *quality*, we compose both the quantity `ringness`, denoting how well the cluster shapes a ring in x,y direction; as well as the quantity `twofold`, denoting how well the cluster resembles two stacked tori in z direction, basically forming a camel-curve in z direction. To break this down to one scalar each, we compute the root mean square (RMS) of the deviations of each localisations radius from the cluster centre (in x,y direction) from the known NPC radius (Lines 20–24). The quantity `twofold` is similarly comprised of a RMS deviation of each localisations z value from the cluster centre (in z direction) from the known NPC height. The mentioned parameters are thus called `npc_radius`, respective `npc_height`.

Figure 3.19 shows a broad overview of the location of the cluster centres (not the localisations within), colour coded by photon count. This should be considered more of a short sanity check than a profound analysis.

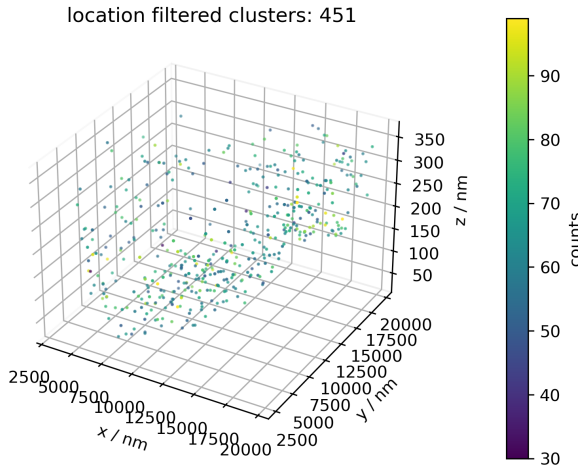


Figure 3.19: 3d plot of the positions of the 451 filtered clusters, colour coded by photon count.

3.5.3 Select Clusters

Now we possess all the information needed to evaluate the list of clusters; for example to sort for the lets say 10 most *ringlike* clusters. Or, by setting `sort = 'ringness + twofold'`, we may find the 10 *best* clusters in terms of both `ringness` and `twofold`—weighted equally—which would comprise the 10 *overall best*, thus *most NPC like* clusters.

For sake of completeness we also include the x , y and z variances, even if they do not comprise a very meaningful parameter in the particular case due to the NPCs geometry.

Figure 3.20 and Figure 3.21 show a 3d plot of the localisations within the 10 *best* clusters, colour coded by photon count respective by cluster assignment.

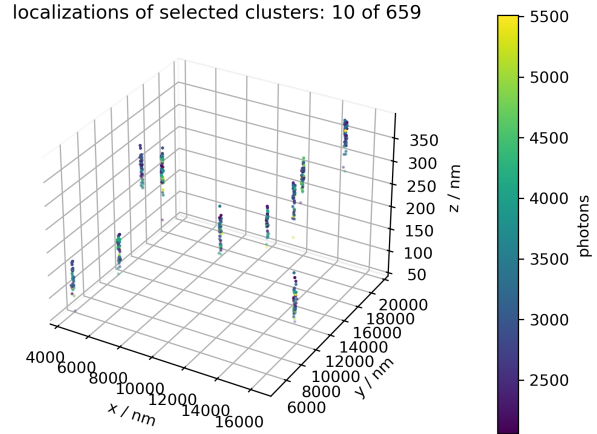


Figure 3.20: 3d plot of the localisations within the 10 best clusters, colour coded by photon count.

localizations of selected clusters: 10 of 659

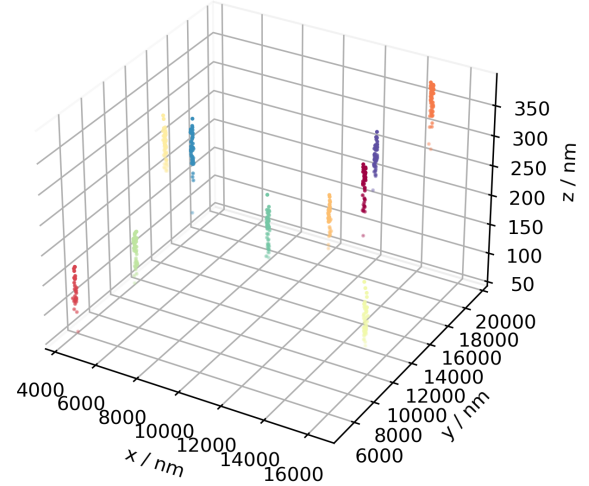


Figure 3.21: 3d plot of the localisations within the 10 best clusters, colour coded by cluster assignment.

3.5.4 X,Y,Z Histograms

As a further sanity check, we plot the histograms for selected clusters (`plot_cluster`), in x , y and z direction; to figure out if the sorting did work effectively—thus the higher sorted

clusters are indeed *better* examples of NPCs.

Figure 3.22 shows exemplary histograms of the x,y (right) respective z distribution (left) of the localisations within the *best* cluster (top), the *worst* (bottom) and one in between.

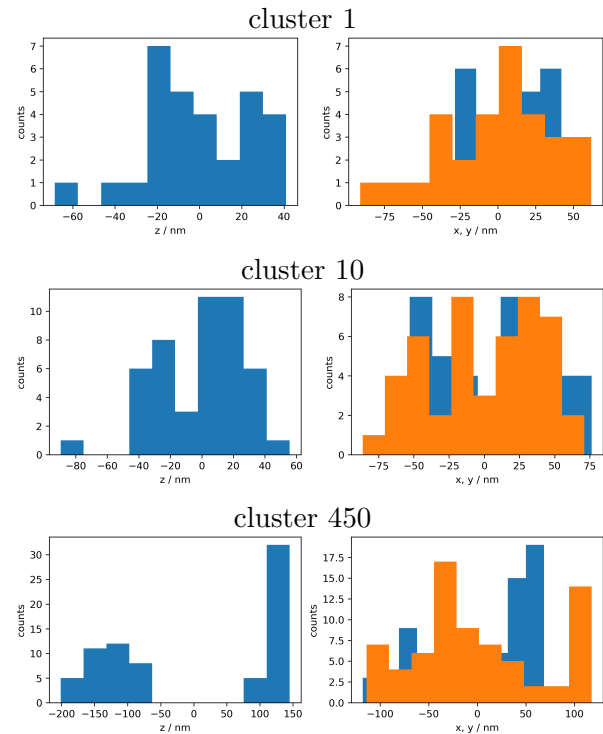


Figure 3.22: histogram of the x,y (right) respective z distribution (left) of the localisations within the best cluster (top), the worst (bottom) and one in between.

In this section I am missing one figure that would show xy and z(x or y) projection of the NPC to really see if we found the right thing

3.6 Dual Colour 3d SMLM

In order to perform two-colour SMLM we marked NPCs and bead samples with an equal amount of both AF488 and AF647 fluorescence dyes.

A first measurement using the Gloxy buffer worked well for the red channel (for which the Gloxy buffer is designed) but did not lead to a good SNR in the blue channel.

Using the OxEA buffer described in Section 2.3.2, we got both channels working, but the overall SNR proved to be not good enough for drift analysis via *ImageJ*, or even particle tracking. There is no way we could try to recover the 3d transformation relating those data sets under this noisy conditions.

Thus we will analyse simulated data instead: based on three dimensional random data sets in Section 3.6.1, as well as based on two dimensional SMLM data sets in Section 3.6.2.

3.6.1 Simulation

In the first and second simulation the transformation relating both sets simply is a translation, respective a rotation and translation (rigid). Examples of sets related in such a way are shown in Figure 3.23 as purple and cyan dots on the top row for solely shifted and in the middle row for shifted and rotated sets (rigid). In a third simulation, the two sets are related by an affine transform adding shearing, reflection and scaling, shown in Figure 3.23 as purple and cyan dots on the bottom row.

All three simulations are now evaluated by both the algorithms `rig()` and `affine()` assuming a rigid respective an affine transformation. The resulting transformation, thus the projection from one set to the other is shown as magenta lines in all six sub figures of Figure 3.23.

The rigid recovery correctly estimates the rigid transforms of the first two simulations

(top and middle row), but fails completely if the point clouds are actually *not* related by a rigid transform (bottom row)!

To test the algorithms stability to noise, the simulations are additionally salted slightly (additive noise to \mathbf{q}). Due to the salt; and the fact, that the positions are pseudo-random points, the resulting transformations are slightly different for every simulation. The below shown comparison should be understood as an example—yet well suited to highlighting common problems.

Shift Projection

For the first simulation (top row), the initially (true) translation vector \mathbf{t}_s^t and rotation matrix \mathbf{R}_s^t is:

$$\mathbf{t}_s^t = \begin{pmatrix} 0 \\ 0.005 \\ 0.003 \end{pmatrix}, \mathbf{R}_s^t = \begin{pmatrix} 1 & 0 & 0 \\ 0 & 1 & 0 \\ 0 & 0 & 1 \end{pmatrix} \quad (3.1)$$

The under rigid assumption (left) recovered translation vector \mathbf{t}_s^r and rotation matrix \mathbf{R}_s^r is:

$$\mathbf{t}_s^r = \begin{pmatrix} 0.0047 \\ 0.0104 \\ 0.0030 \end{pmatrix}, \mathbf{R}_s^r = \begin{pmatrix} 0.999 & 0.000 & 0.000 \\ 0.000 & 0.999 & 0.000 \\ 0.000 & 0.000 & 0.999 \end{pmatrix} \quad (3.2)$$

The under affine assumption (right) recovered translation vector \mathbf{t}_s^a and rotation matrix \mathbf{R}_s^a is:

$$\mathbf{t}_s^a = \begin{pmatrix} 0.0050 \\ 0.0108 \\ 0.0030 \end{pmatrix}, \mathbf{R}_s^a = \begin{pmatrix} 1.000 & 0.000 & 0.301 \\ 0.000 & 0.999 & -0.148 \\ 0.000 & 0.000 & 1.001 \end{pmatrix} \quad (3.3)$$

Rigid Projection

For the first simulation (top row), the initially (true) translation vector \mathbf{t}_r^t and rotation ma-

trix \mathbf{R}_r^t is:

$$\mathbf{t}_r^t = \begin{pmatrix} 0 \\ 0.005 \\ 0.003 \end{pmatrix}, \mathbf{R}_r^t = \begin{pmatrix} 0.342 & 0 & -0.940 \\ 0 & 1 & 0 \\ 0.940 & 0 & 0.342 \end{pmatrix} \quad \mathbf{t}_a^a = \begin{pmatrix} -0.0058 \\ 0.0110 \\ -0.0129 \end{pmatrix}, \mathbf{R}_a^a = \begin{pmatrix} -0.684 & -0.342 & -0.566 \\ 0.000 & 1.000 & -0.319 \\ -1.879 & -0.940 & 1.364 \end{pmatrix} \quad (3.4)$$

The under rigid assumption (left) recovered translation vector \mathbf{t}_r^r and rotation matrix \mathbf{R}_r^r is:

$$\mathbf{t}_r^r = \begin{pmatrix} 0.0017 \\ 0.0103 \\ 0.0077 \end{pmatrix}, \mathbf{R}_r^r = \begin{pmatrix} 0.342 & 0.000 & -0.940 \\ 0.000 & 9.999 & 0.000 \\ 0.940 & 0.000 & 0.342 \end{pmatrix} \quad (3.5)$$

The under affine assumption (right) recovered translation vector \mathbf{t}_r^a and rotation matrix \mathbf{R}_r^a is:

$$\mathbf{t}_r^a = \begin{pmatrix} 0.0014 \\ 0.0093 \\ 0.0069 \end{pmatrix}, \mathbf{R}_r^a = \begin{pmatrix} 0.3420 & 0.000 & -0.614 \\ 0.000 & 9.999 & 1.014 \\ 0.940 & 0.000 & 1.235 \end{pmatrix} \quad (3.6)$$

Affine Projection

For the first simulation (top row), the initially (true) translation vector \mathbf{t}_a^t and rotation matrix \mathbf{R}_a^t is:

$$\mathbf{t}_a^t = \begin{pmatrix} 0 \\ 0.005 \\ 0.003 \end{pmatrix}, \mathbf{R}_a^t = \begin{pmatrix} -0.684 & -0.342 & -0.940 \\ 0.000 & 1.000 & 0.000 \\ -1.879 & -0.940 & 0.342 \end{pmatrix} \quad (3.7)$$

The under rigid assumption (left) recovered translation vector \mathbf{t}_a^r and rotation matrix \mathbf{R}_a^r is:

$$\mathbf{t}_a^r = \begin{pmatrix} 0.0113 \\ 0.0059 \\ 0.0341 \end{pmatrix}, \mathbf{R}_a^r = \begin{pmatrix} -0.325 & -0.106 & -0.940 \\ -0.309 & 0.951 & 0.000 \\ -0.894 & -0.290 & 0.342 \end{pmatrix} \quad (3.8)$$

The under affine assumption (right) recovered translation vector \mathbf{t}_a^a and rotation matrix

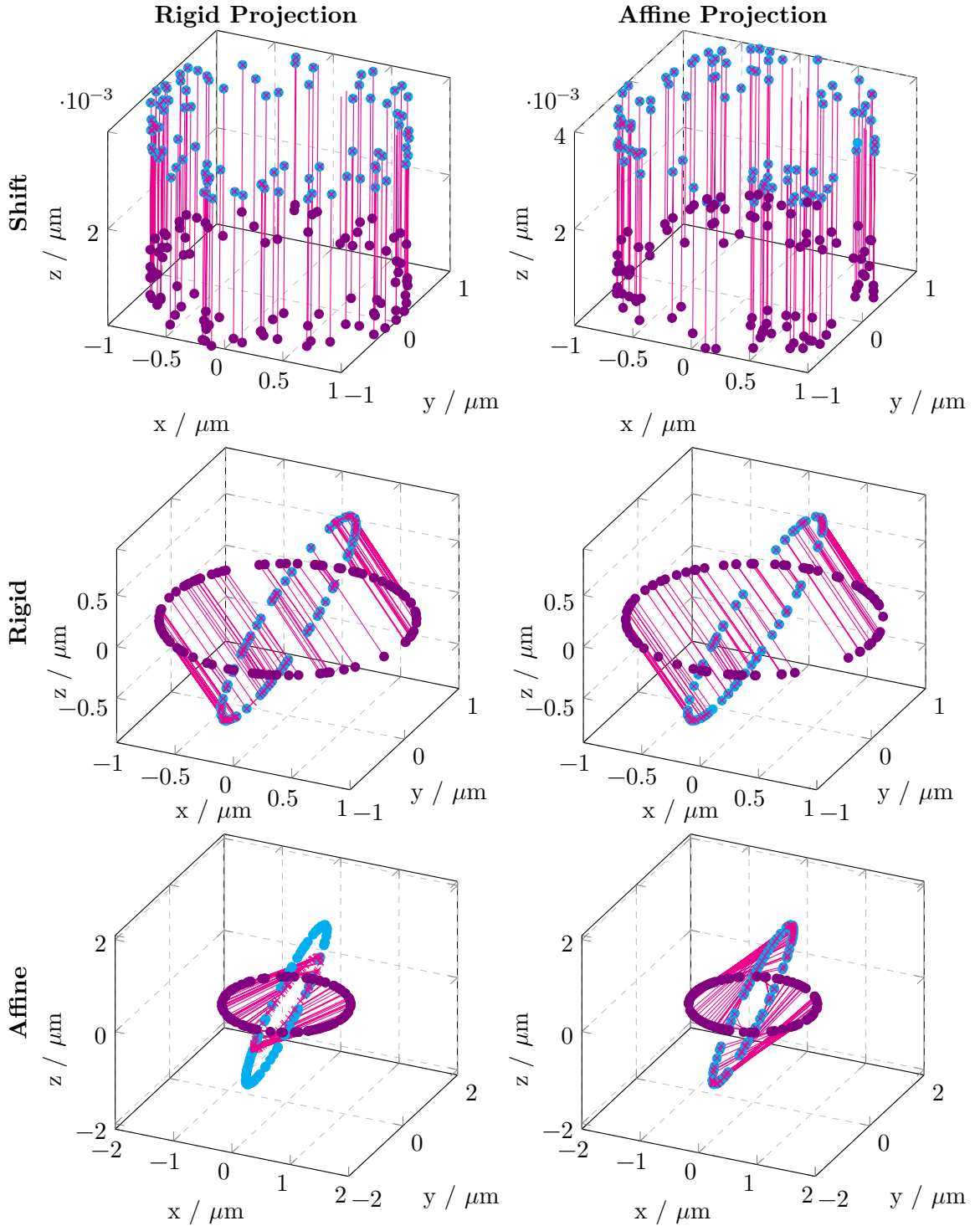


Figure 3.23: Demonstration of the recovery of rigid (left) respective affine (right) transformations, via recovering localisations of simulated two channel SMLM data; transformation (magenta) from red channel (violet) to blue channel (cyan); for the use cases of translation (top), rigid transformation (middle) and affine transformation (bottom). Obviously a rigid transformation may not correctly reconstruct an affine transformed data set (bottom left).

3.6.2 Projected 2d NPC

Lacking proper 3d dual colour SMLM data, we choose to use two-dimensional *Thunder-STORM* SMLM data for a second proof of work.

A close look on such generated sets already shows interesting behaviour: the two sets are *shifted*. Obviously by utilising different wavelength regimes in a highly wavelength dependent process (optical path, refraction, objective, PSF, etc), one will eventually face some offset.

Rigid Projection

The rigid recovery worked quite flawlessly, the mean rotation matrix $\bar{\mathbf{R}}_r$ is almost unity within uncertainty. The mean translation vector $\bar{\mathbf{t}}_r$ shows a good variance over all the twelve analysed sets, with mean and standard deviation of:

$$\bar{\mathbf{t}}_r = \begin{pmatrix} 39 \\ 30 \\ 0 \end{pmatrix} \pm \begin{pmatrix} 10 \\ 4 \\ 0 \end{pmatrix} \mu\text{m} \quad (3.10)$$

$$\bar{\mathbf{R}}_r = \begin{pmatrix} 1.0000 & 0.0008 & 0 \\ -0.0008 & 1.000 & 0 \\ 0 & 0 & 1 \end{pmatrix} \quad (3.11)$$

$$\sigma(\mathbf{R}_r) = \begin{pmatrix} 4 \cdot 10^{-7} & 4 \cdot 10^{-4} & 0 \\ 4 \cdot 10^{-4} & 4 \cdot 10^{-7} & 0 \\ 0 & 0 & 0 \end{pmatrix} \quad (3.12)$$

As an example of this rigid transformation, the localisations of the blue channel (blue \times), the red channel (violet $+$) and the projection from blue channel to red channel channel (magenta \circ) is shown in Figure 3.24, for one exemplary data set. The transformed blue channel localisations mostly align well with the red channel localisations.

Affine Projection

A similar analysis assuming an affine transformation though fails completely. This is due to the fact that the data sets are projected onto the z plane for analysis, so are now composing strictly parallel planes. This leads to the covariance matrices being *singular*, so the affine transform routine fails (or at least heavily crashes trying) to invert the covariance matrices. At least the results are so horribly wrong—if at all—that it is highly unlikely to *not* get suspicious immediately. In our case the translation vector is in the order of millimeters, which is not very plausible for two sets within the same cell. Thus we omitted the results.

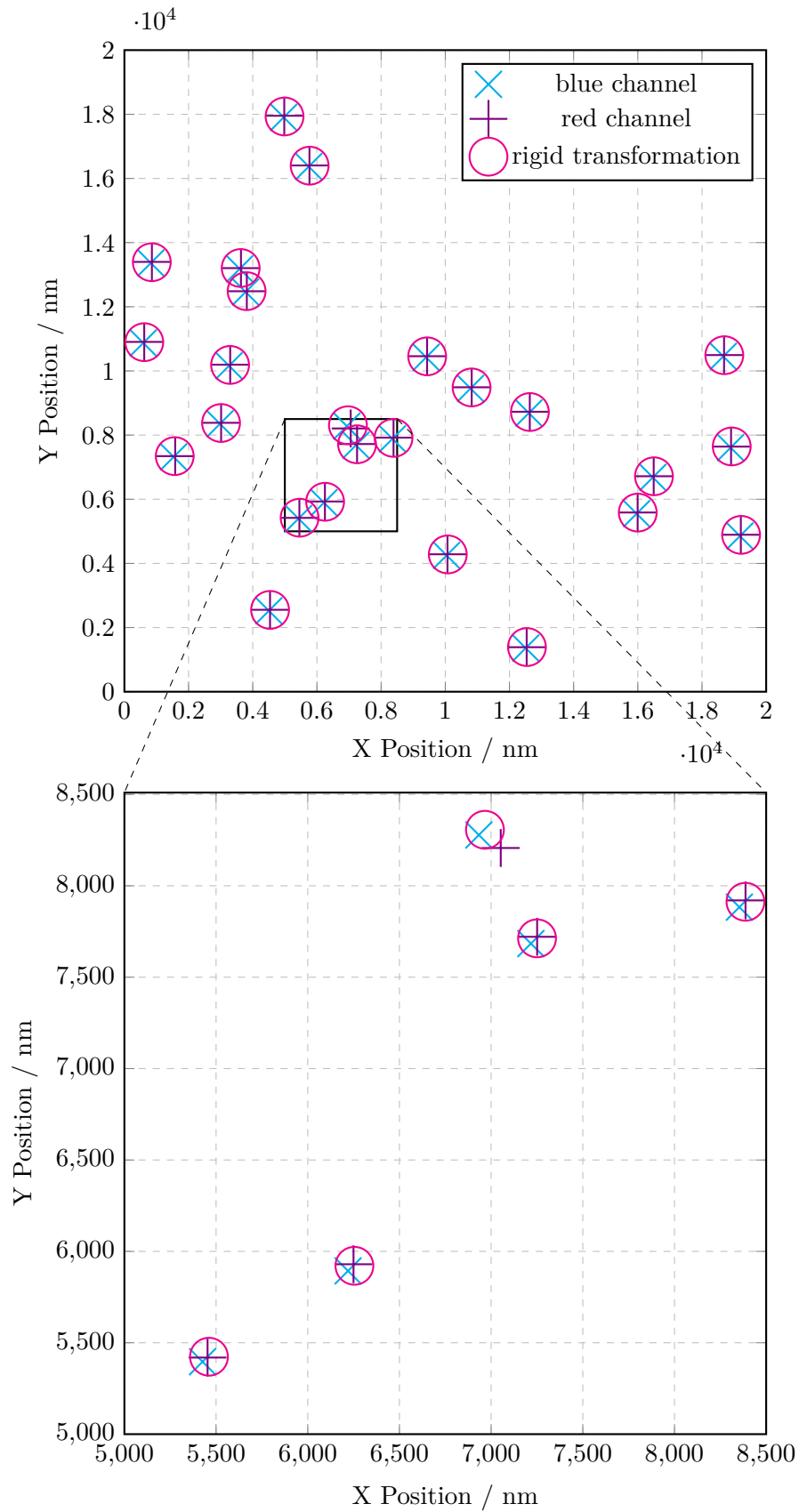


Figure 3.24: Demonstration of a rigid transformation of the localisations (magenta \circ) from blue channel (blue \times) to red channel ($+$); the transformed blue channel localisations mostly align well with the red channel localisations.

Chapter 4

Discussion & Conclusion

4.1 Dual Colour Optics

4.1.1 Zernike Modes

The ZERNIKE modes for both red and blue channel are estimated via phase retrieval of in-focus measurements of beads at various depths. This yields a full PSF model to be used for defocus 3d SMLM.

The image stacks look good, even if not all are perfectly symmetrical—some errors are to be expected.

The estimated ZERNIKE modes of the PSF are mostly plausible; based on the modes and the order of magnitude.

This is further backed by the comparison of the results grouped by the three correction collar settings $\{0.13, 0.17, 0.19\}$, in Figure 3.3, Figure 3.4 and Figure 3.5. It is quite obvious, that the results for both red and blue channel are in the same order of magnitude—if not quite similar—for most of the ZERNIKE modes.

Yet the phase retrieval program gave the error *high residual error* for both the red and the blue channel when using the correction collar settings $\{0.17, 0.19\}$. This error indicates that the obtained images are distorted in a way the phase retrieval program cannot perceive and correct for. There might be many different

reasons for that, a thorough inspection of the theoretical background of the given phase retrieval program far exceeds the scope of this work. But since the correction setting is solely meant for enhancing the resulting images (less distortion), we can conclude that the settings $\{0.17, 0.19\}$ do not work in this way. Even if the setting of 0.17 is recommended by the manufacturer for our microscope, this might not give the best results in our downstream pipeline, and the setting of 0.13 should be used nevertheless.

4.1.2 Correction Collar

Based on the Figures 3.7 and Figure 3.8, and considering the fact—that we are interested in moderately defocusing (up to say 250 nm)—one might conclude, that the most preferable setting for the correction collar is 0.13.

Yet the recommended setting for our microscope setup is 0.17! Based on the PSF stacks one would have guessed the 0.17 is more sensitive to z since it changes much more with different z positions than 0.13.

As a conclusion we propose The best setting of the correction collar for the Olympus 1.5 NA objective is shown to be 0.13. Here we find the preferable compromise between x,y precision and z precision, in the regime between about 0

and 250 nm.

4.2 Three Dimensional SMLM

The analysis performed in Section 3.4 is well suited to greatly reduce the localisations, just by omitting unphysical data and noise; in our example from initially 370k to below 100k, or to about 26%.

4.3 NPC Analysis

Our approach of fully automatic evaluation of the NPC *quality*, may well be considered failed.

Nevertheless we might have gained some valuable insight, as some of the results of the NPC analysis might still prove themselves useful as a secondary filters.

4.3.1 Define Scalar Quality

The fully automatic evaluation of the NPC *quality*, shown in Section 3.5 surfaced mixed results. The key problems being for one, that there are quite many parameters involved; and secondly that the analysis proved very susceptible to changes of most of these parameters.

A quick glance at the histograms in Section 3.5.4 shows, that the cluster considered to be the *best* does not look better in fact, than most of the other clusters. We may well consider this approach failed.

Nevertheless we might have gained some valuable insight, into why this approach doesn't work. Reasons for this may be any and all of the following, for some of which we may suggest possible improvements.

numbers The clusters consist of very few localisations each, statistical analysis of

so few elements have to be considered shaky. More constituents within each cluster would probably make this analysis more reliable.

quality The definitions of the two quality entities **ringness** and **twofold**, might not be derived well using RMS. A more sophisticated approach to quantify the clusters deviations to our known NPC geometry might work better, such as fitting the histogram in z direction to a GAUSSIAN.

weighting The equal weighting of **ringness** and **twofold** quantities are canceling each other; Some clusters might look very *ring-like*, but are not at all stacked on top of each other, and vice versa. Unequal weighting based on empirical fine tuning might lessen this problem, but will most likely not solve it.

4.3.2 Secondary Filter

Some of the results of the NPC analysis might still prove themselves useful as a secondary filters. In reducing the clusters until only a few remain, effectively also finds the *best*.

high variance One might want to exclude clusters with an overly high variance, as these might be in fact two NPCs too close to each other to be accounted separately by the clustering algorithm.

low variance Quite similarly we might exclude those clusters showing extremely low variance, under suspicion of being well concentrated—yet noise, not representing a NPC at all.

spread Likewise we may exclude clusters spreading far in z, due to our knowledge of the NPC height, as well as in x,z due to the NPCs well defined radius.

In the end, possessing a list of the clusters position allows for a much easier way to plot some of them manually, than to zoom in on a plot of thousands of localisations repeatedly.

4.4 Dual Colour Buffer

The prepared samples, both beads and NPCs have been evaluated using Gloxy buffer and OxEA buffer.

The two channels (red and blue) showed great differences in blinking speed, *dark state* and *bright state* lifetime, Signal and background magnitude as well as SNR.

The data obtained from this dual colour three dimensional localisation was not of high enough precision to be analysed meaningfully. We thus propose further investigation in buffers used for dual colour SMLM.

4.5 Dual Colour Projection

Simply put, the algorithm `rig()` finds the *best* rigid transformation, whatever the real relation is. This poses a serious caveat for experimental data, since one is usually not in possession of any form of ground truth to check whether the result is plausible or not.

4.5.1 SMLM Simulations

At first glance at the plots in Figure 3.23, the rigid as well as the shift problem (top and middle row) are similarly well solved either by rigid or affine assumption; their projection of the set q neatly correspond with set p . Also quite obviously the recovery of a assumed rigid transform of sets *not* related in such a way (bottom row) does not yield a significant solution.

A closer inspection of the respective recovered translation vectors \mathbf{t} and rotation matri-

ces \mathbf{R} in Section 3.6 enables a deeper understanding of the involved misconceptions—that ultimately question this approach.

Shift

Comparison of the respective recovered translation vectors $\mathbf{t}_s^{r,a}$ and rotation matrices $\mathbf{R}_s^{r,a}$ to the ground truth \mathbf{t}_s^t and \mathbf{R}_s^t show, that both sort of agree—for solely shifted data sets. The affine projection is a little farther off.

Rigid

Comparison of the respective recovered translation vectors $\mathbf{t}_r^{r,a}$ to the ground truth \mathbf{t}_r^t shows, that even the rigid recovery does not represent the ground truth well, with the affine projection being even farther off still.

Yet a comparison of the respective recovered rotation matrices $\mathbf{R}_r^{r,a}$ to the ground truth \mathbf{R}_r^t show good agreement for the rigid recovery. The affine recovery is slightly off, but somewhat acceptable.

Affine

Comparison of the respective recovered translation vectors $\mathbf{t}_a^{r,a}$ to the ground truth \mathbf{t}_a^t show very little agreement for both the rigid and the affine recovery.

A comparison of the respective recovered rotation matrices $\mathbf{R}_a^{r,a}$ to the ground truth \mathbf{R}_a^t shows show good agreement for the affine recovery, with the rigid recovery completely failing.

4.6 Dual Colour Simulation

Concluding, one best uses an rigid recovery for a rigid problem, or an affine recovery for an affine problem, as shown in Table 4.1 and Table 4.2.

Table 4.1: Quality of the recovered rotation translation vectors (transformation) matrices $\mathbf{t}_{s,r,a}^{r,a}$.

Problem	rig()	affine()
Shift	ok	ok
Rigid	bad	bad
Affine	worse	bad

Table 4.2: Quality of the recovered rotation (transformation) matrices $\mathbf{R}_{s,r,a}^{r,a}$

Problem	rig()	affine()
shift	ok	ok
rigid	good	bad
affine	worse	good

Due to the convexity of the problem (there are infinitely many transformations), the recovery of a translation vector under the assumption of at least dome rotation involved is not really possible, as shown in Table 4.1 and Table 4.2. This poses a dangerous caveat for the dual colour SMLM analysis, where we cannot rule out rotations.

4.6.1 Projected 2d NPC

As a second proof of work, we tested both rigid and affine recovery on several real dual colour SMLM data sets of two colour in focus measurements of different cells successively recorded in the same sample.

Mind that this is a simulation, the actual transformation between both sets using the SMLM analysis might look completely different.

Rigid

The rigid recovery worked quite flawlessly, the mean rotation matrix $\bar{\mathbf{R}}_r$ is almost unity

within uncertainty. Yet the mean translation vector $\bar{\mathbf{t}}_r$ shows a high variance (at least on x axis) over all the twelve analysed sets, with mean and standard deviation of:

$$\bar{\mathbf{t}}_r = \begin{pmatrix} 39 \\ 30 \\ 0 \end{pmatrix} \pm \begin{pmatrix} 10 \\ 4 \\ 0 \end{pmatrix} \mu\text{m} \quad (4.1)$$

$$\bar{\mathbf{R}}_r = \begin{pmatrix} 1.0000 & 0.0008 & 0 \\ -0.0008 & 1.000 & 0 \\ 0 & 0 & 1 \end{pmatrix} \quad (4.2)$$

$$\sigma(\mathbf{R}_r) = \begin{pmatrix} 4 \cdot 10^{-7} & 4 \cdot 10^{-4} & 0 \\ 4 \cdot 10^{-4} & 4 \cdot 10^{-7} & 0 \\ 0 & 0 & 0 \end{pmatrix} \quad (4.3)$$

Affine

A similar analysis assuming an affine transformation though fails completely, this method simply cannot work on two dimensional data.

Appendix A

Code

A.1 3d SMLM Analysis: NPC

A.1.1 Import

```
1  #@markdown ##import core
2  import pandas as pd
3  import matplotlib.pyplot as plt
4  import numpy as np
5  import matplotlib as mpl
6  from mpl_toolkits.mplot3d import Axes3D
7  import scipy.io
8  from sklearn.cluster import DBSCAN
9  from sklearn import metrics
10 from sklearn.datasets import make_blobs
11 from sklearn.preprocessing import StandardScaler
12
13 #@markdown ##import jupyter
14 #%%matplotlib ipympl
15 #%%matplotlib widget
16 #%%matplotlib interactive
17 %matplotlib inline
18 import trackpy
19 #import sdt
20 #from sdt import io, chromatic, multicolor, brightness
21
22 ## local
23 wd = 'data/210422_npc_red_defocus/'
24 data = pd.read_csv( wd + 'cell1_tr1000_def500.csv',
25 header = None,
26 names=[ "x", "y", "z", "n", "bg","fit","id","frame"] )
```

A.1.2 Drift Correction

```
1  #@markdown ## import & scale drift
2  #@markdown > set **magnification** via factor in drift.
3
4  drift = pd.read_csv( wd + 'day2_cell1_driftValues.csv')
5
6  drift['Y2']=drift['Y2']*146.6
7  drift['Y3']=drift['Y3']*146.6
8  drift['X2']=np.round(drift['X2'])
9  drift['X3']=np.round(drift['X3'])
10
11 #@markdown ## apply drift correction
12
13 for i in range(len(drift)-1):
14     fr=data[(data['frame']>=drift['X2'].iloc[i]) &
15             (data['frame']<drift['X2'].iloc[i+1])]
16     fr['y']=fr['y']-drift['Y2'].iloc[i]
17     fr['x']=fr['x']-drift['Y3'].iloc[i]
18     data[(data['frame']>=drift['X2'].iloc[i]) &
19             (data['frame']<drift['X2'].iloc[i+1])]=fr
```

A.1.3 Photon Counts

```
1  #@markdown ## Check: photon counts
2  #@markdown > set `max_photons` accordingly (default: 10000).
3  max_photons = 10000 #@param {type:"slider", min:0, max:40000, step:1000}
4
5  fig = plt.figure()
6  plt.hist( data['n'], bins=50, range=( 0, max_photons ) )
```

A.1.4 Filter

```
1  #@markdown ## filter
2  #@markdown > set `min_photons` and `max_photons` accordingly (default: 2000
3  ↵   < photons < 7000). \
4  #@markdown > set `min_z` and `max_z` accordingly (default: 0 < z < 499). \
5  #@markdown > set `min_fit` accordingly (default: 6e6).
6  min_photons = 2000 #@param {type:"slider", min:0, max:40000, step:1000}
7  max_photons = 7000 #@param {type:"slider", min:0, max:40000, step:1000}
8  min_z = 0 #@param {type:"slider", min:0, max:500, step:1}
9  max_z = 384 #@param {type:"slider", min:0, max:500, step:1}
10 min_fit = 7192000 #@param {type:"slider", min:0, max:1e7, step:1000}
```

```

11 fdata = data[ ( data['n'] > min_photons ) &
12   ( data['n'] < max_photons ) &
13   ( data['z'] > min_z ) &
14   ( data['z'] < max_z ) &
15   ( data['fit'] < min_fit ) ]

```

A.1.5 Track Particles

```

1  #@markdown ## track all in x,y
2  #@markdown > set `sr` to wanted search range (default: 50). \
3  #@markdown > set `mem` to wanted memory (default: 10).
4  sr = 50 #@param {type:"slider", min:0, max:100, step:1}
5  mem = 10 #@param {type:"slider", min:0, max:100, step:1}
6
7  linkedxy = trackpy.link_df( fdata,
8    pos_columns = ["x", "y", "z"],
9    search_range = sr,
10   memory = mem )
11
12  particles = linkedxy.groupby( "particle" ).aggregate( np.mean )
13  std_pos = linkedxy.groupby( "particle" ).aggregate( 'std' )
14  particles["length"] = linkedxy.groupby( "particle" ).apply( len )
15  particles["z_std"] = std_pos['z'].copy()
16  particles["x_std"] = std_pos['x'].copy()
17  particles["y_std"] = std_pos['y'].copy()

```

A.2 3d SMLM Analysis: NPC

A.2.1 Clustering

```
1  #@markdown ## compute dbSCAN
2  #@markdown > set `dim = 2` for clustering in x and y (default:).\
3  #@markdown > set `dim = 3` for experimental clustering in 3d; be aware that
4  ↪ x, z and y precision probably vary!\
5  #@markdown > set `eps` (default: 200).\
6  #@markdown > set `min_samples` (default: 10).
7  dim = "2" #@param [2, 3]
8  eps = 100 #@param {type:"slider", min:0, max:500, step:10}
9  min_samples = 50 #@param {type:"slider", min:1, max:100, step:1}
10
11 alocalisations = localisations.to_numpy()
12 alocalisations[ :, 0:2 ]
13
14 db = DBSCAN( eps, min_samples ).fit( alocalisations[ :, 0:int( dim ) ] )
15 core_samples_mask = np.zeros_like( db.labels_, dtype=bool )
16 core_samples_mask[ db.core_sample_indices_ ] = True
17 labels = db.labels_
18 localisations[ "cluster" ] = labels
19
20 # count clusters (ignore noise if present)
21 n_clusters_ = len( set( labels ) ) - ( 1 if -1 in labels else 0 )
22 n_noise_ = list( labels ).count( -1 )
23
24 #print('Estimated number of clusters: %d' % n_clusters_)
25 #print('Estimated number of noise points: %d' % n_noise_)
26
27 nlocalisations = localisations.loc[ localisations['cluster'] == -1 ]
clocalisations = localisations.loc[ localisations['cluster'] != -1 ]
```

A.2.2 Cluster Analysis

```
1  #@markdown ## analyse clusters
2  #@markdown > set `npc_radius` to NPC radius /nm (default: 50).\
3  #@markdown > set `npc_height` to NPC height /nm (default: 150).
4  npc_radius = 50 #@param {type:"slider", min:0, max:500, step:1}
5  npc_height = 25 #@param {type:"slider", min:0, max:500, step:1}
6
7  clabels = set(labels)
8  cnames = [ "counts", "xmean", "ymean", "zmean", "nmean", "xvar", "yvar",
9  ↪ "zvar",
```

```

9      "nvar", "label", "ringness", "twofold" ]
10     clusters = pd.DataFrame( index = clabels, columns = cnames, dtype="float64"
11       )
12     clusters[ "label" ] = clabels
13
14     for k in clabels:
15       tmp = localisations.loc[ localisations['cluster'] == k ]
16       clusters.loc[ k, "counts" ] = len( tmp )
17       for label in [ "x", "y", "z", "n" ]:
18         clusters.loc[ k, label+"mean" ] = np.mean( tmp.loc[ :, label ] )
19         clusters.loc[ k, label+"var" ] = np.var( tmp.loc[ :, label ] )
20
21     ## xy: radius (distance to centroid)
22     rad = np.sqrt( ( tmp.loc[ :, "x" ] - clusters.loc[ k, "xmean" ] )**2 +
23     ( tmp.loc[ :, "y" ] - clusters.loc[ k, "ymean" ] )**2 )
24     ## xy: radius rms deviation from NPC radius
25     clusters.loc[ k, "ringness" ] = np.sqrt( sum( ( rad - npc_radius )**2 ) )
26
27     ## z: radius (distance to centroid)
28     rad = abs( tmp.loc[ :, "z" ] - clusters.loc[ k, "zmean" ] )
29     ## z: radius rms deviation from NPC radius
30     clusters.loc[ k, "twofold" ] = np.sqrt( sum( ( rad - npc_height )**2 ) )
31
32     #@markdown ## filter clusters
33     #@markdown > set `count_threshold` to min elements (counts) in cluster
34     #> (default: 30)\n
35     #@markdown > set `diameter_threshold` to max x,y (radius) deviation of
36     #> cluster from NPC diameter (default: 200)\n
37     #@markdown > set `twofold_threshold` to max z (radius) deviation of cluster
38     #> from NPC height (default: 200)\n
39     #@markdown > set `xyvar_threshold` to wanted x,y variance (default: 1e4)\n
40     #@markdown > set `zvar_threshold` to wanted z variance (default: 1e4)
41     count_threshold = 100 #@param {type:"slider", min:0, max:200, step:1}
42     diameter_threshold = 500 #@param {type:"slider", min:0, max:500, step:10}
43     twofold_threshold = 1000 #@param {type:"slider", min:0, max:1000, step:10}
44     xyvar_threshold = 100000 #@param {type:"slider", min:0, max:1e5, step:1e3}
45     zvar_threshold = 100000 #@param {type:"slider", min:0, max:1e5, step:1e3}
46
47     fclusters = clusters[ ( clusters['counts'] < count_threshold ) &
48     ( clusters['ringness'] < diameter_threshold ) &
49     ( clusters['twofold'] < twofold_threshold ) &
50     ( clusters['xvar'] < xyvar_threshold ) &
51     ( clusters['yvar'] < xyvar_threshold ) &

```

```
48 ( clusters['zvar'] < zvar_threshold ) ]
```

A.2.3 Select Clusters

```
1  #@markdown ## select best clusters & plot localisations
2  #@markdown > set `show_clusters` to wanted number of best clusters
3  ↳ (default: 100).\
4  #@markdown > set `sort` to sort the best clusters (default: ringness +
5  ↳ twofold).
6  show_clusters = 10 #@param {type:"slider", min:0, max:1000, step:1}
7  sort = 'ringness + twofold' #@param [ "ringness + twofold", "twofold",
8  ↳ "ringness", "xyvar" , "xvar" ]
9
10 if sort == "xvar": # sort by variance
11     sclusters = fclusters.sort_values( "xvar" )
12 elif sort == "xyvar": # sort by x and y variance using least squares
13     sclusters = fclusters.loc[
14         ( fclusters.xvar ** 2 + fclusters.yvar ** 2 ).sort_values().index ]
15 elif sort == "ringness": # sort by ringness (deviation to ringness)
16     sclusters = fclusters.sort_values( "ringness" )
17 elif sort == "twofold": # sort by ringness (deviation to ringness)
18     sclusters = fclusters.sort_values( "twofold" )
19 elif sort == "ringness + twofold": # sort by ringness (deviation to
20     ↳ ringness)
21     sclusters = fclusters.loc[
22         ( fclusters.twofold ** 2 + fclusters.ringness ** 2 ).sort_values().index ]
23
24 show_clusters = min( show_clusters, len( sclusters ) )
25 selected_clusters = sclusters["label"].iloc[ 0:show_clusters ]
26
27 fig = plt.figure()
28 ax = fig.add_subplot( projection = '3d' )
29 for clus in selected_clusters:
30     flocalisations = localisations[ ( localisations['cluster'] == clus ) ]
31     ff = ax.scatter( flocalisations['x'],
32                     flocalisations['y'],
33                     flocalisations['z'],
34                     s=1 ,c = flocalisations['n'] )
```

A.2.4 X,Y,Z Histograms

```
1  #@markdown ## Check: z distribution
2  #@markdown > set `plot_cluster` to wanted cluster (default: 0).
```

```

3   plot_cluster = 3  # @param {type:"slider", min:0, max:100, step:1}
4   plot_cluster = min( plot_cluster, len( sclusters ) -1 )
5
6   tmp = localisations.loc[ localisations['cluster'] ==
7     sclusters.loc[ sclusters.index[ plot_cluster ],
8     "label" ] ]
9
10  z = tmp.z - np.mean( tmp.z )
11
12  fig, axes = plt.subplots(2, 1, figsize=(4, 7) ) # figsize=(4, 12)
13
14  axes[0].hist( tmp.z - np.mean( tmp.z ) )
15  axes[0].set_xlabel('z / nm')
16  axes[0].set_ylabel('counts')
17  #axes[0].set_title( 'z' )
18
19  axes[1].hist( tmp.x - np.mean( tmp.x ) )
20  axes[1].hist( tmp.y - np.mean( tmp.y ) )

```

A.3 Dual Colour 3d SMLM

A.3.1 Cockpit: cockpit.m

```
1 #!/bin/octave
2 ## images fluorescence microscopy / 3d position / offsets.
3 ## splice red/green/blank fluorescence microscopy images already located
4 ## into red/green matrices for further analysis, find rigid transform,
5 ## do statistics on all files.
6 ## @ moritz siegel
7
8 ## init
9 close all
10 clear all
11 clc
12 graphics_toolkit('gnuplot')
13 #graphics_toolkit('qt')
14 #graphics_toolkit('fltk')
15
16 ##
17 ## soft settings
18 global hd = "~/biophysics" # parent directory
19 global wd = "data/210318_beads_2_colors_in_focus"
20 global fn = "position"
21 global nn = ""; # additional luminosity suffix ( default: "" )
22 method = "rigid"; # /char, "rigid", "affine", method to reconstruct
23 global minpts = 10; # minimum number of points needed in its neighbourhood to
24 # consider it as a valid data(not noise). ( default: 3 )
25 global dist = 300; #/nm, distance on which neighbourhood is calculated.
26 # default: 200 )
27 nmax = 15; #/num, maximum number of files analysed. ( default: 10 )
28 global verbose = true; # /bool, plot for error checking? ( default: true )
29 exclude = [ 6, 7, 8, 11, 12 ]
30 channel_order0 = [ 0, 1, 2 ];
31 channel_order = repmat( channel_order0, nmax, 1 );
32 channel_order( 3, : ) = [ 2, 0, 1 ];
33 channel_order( 4, : ) = [ 1, 2, 0 ];
34 channel_order( 6, : ) = [ 2, 0, 1 ];
35 channel_order( 7, : ) = [ 1, 2, 0 ];
36 channel_order( 8, : ) = [ 2, 0, 1 ];
37 channel_order( 12, : ) = [ 2, 0, 1 ];
```



```

71 ## save optimal rigid transform for comparison
72 rotations( n, :, : ) = rotation;
73 translations( n, : ) = translation;
74 endfor

```

A.3.2 Splice Channels: ampel.m

```

36     empty( ne, : ) = pos( k, : );
37     ne = ne + 1;
38     case channel_order(3)
39         red( nr, : ) = pos( k, : );
40         nr = nr + 1;
41     endswitch
42 endfor
43 disp( sprintf( 'sorted localisations:\n %d red\n %d blue\n %d empty', nr,
44     ↵ nb, ne ) );
44 fprintf( rf, 'sorted localisations:\n %d red\n %d blue\n %d empty\n', nr,
45     ↵ nb, ne );
46
46 ## analyse clusters & average centroids.
47 [ assignments_blue, c_blue ] = dbscan( blue( 1:300, 3:4 ), minpts, dist );
48 for k = 1 : c_blue
49     idx = find( assignments_blue == k );
50     centroid_blue( k, 1:2 ) = mean( blue( idx, 3:4 ), 1 );
51 endfor
52 [ assignments_red, c_red ] = dbscan( red( 1:300, 3:4 ), minpts, dist );
53 for k = 1 : c_red
54     idx = find( assignments_red == k );
55     centroid_red( k, 1:2 ) = mean( red( idx, 3:4 ), 1 );
56 endfor
57
58 ## need to ditch clusters if the sets are not equally sized.
59 assert( c_red == c_blue, "clusters are not equally sized" );
60
61 ## recover transform.
62 switch( method )
63     case "rigid"
64         ## we only have 2d data currently, introduce linear dependent z
65         ↵ component.
66         centroid_red = [ centroid_red, zeros( c_red, 1 ) ]
67         centroid_blue = [ centroid_blue, zeros( c_blue, 1 ) ]
68         [ rotation, translation ] = rig( centroid_blue, centroid_red )
69     case "affine"
70         ## we only have 2d data currently, introduce noise for z component,
71         ## matrix cant be singular, else cholesky decomposition fails.
72         z = 1 + 1e-3 * rand( c_red, 1 );
73         centroid_red = [ centroid_red, z ];
74         centroid_blue = [ centroid_blue, z ];
75         [ rotation, translation ] = affine( centroid_blue, centroid_red );
76     endswitch

```

```

77 ## transform blue set to red set.
78 centroid_blue_transformed = ( rotation * centroid_blue' )' + translation;
79
80 endfunction

```

A.3.3 Rigid Transformation: rig.m

```

1 #!/bin/octave
2 function [ rotation, translation, s ] = rig( p, q )
3 ## this function "rig(p,q)" finds the optimal rigid transform in
4 ## 3-dimensional euclidian space, using least squares and
5 ## single-value-decomposition. Given a 3xn matrix (set of n 3d
6 ## positions), it returns the rotation matrtix "rotation", and the
7 ## translation vector "translation".
8 ##
9 ## K. S. Arun, T. S. Huang and S. D. Blostein, "Least-Squares Fitting of
10 ## Two 3-D Point Sets," in IEEE Transactions on Pattern Analysis and
11 ## Machine Intelligence, vol. PAMI-9, no. 5, pp. 698-700, Sept. 1987,
12 ## doi: 10.1109/TPAMI.1987.4767965.
13 ##
14 ## moritz siegel @ 210322
15
16 ## check stuff.
17 assert( nargin == 2 && size( p ) == size( q ), ...
18 "need 2 identical input matrices\n" );
19 assert( size( p, 2 ) == 3, "input matrix p must be nx3\n" );
20 assert( size( q, 2 ) == 3, "input matrix q must be nx3\n" );
21 n = size( p, 1 );
22 assert( n > 2, "need at least 3 points\n" );
23
24 ## 1) center to get rid of translation.
25 centroid_p = mean( p, 1 );
26 centroid_q = mean( q, 1 );
27 p_shifted = p - repmat( centroid_p, n, 1 );
28 q_shifted = q - repmat( centroid_q, n, 1 );
29
30 ## 2) solve least squares problem for best rotation.
31 ## -----
32
33 ## covariance matrix.
34 h = p_shifted' * q_shifted;
35
36 ## singular value decomposition.

```

```

37 [ u, s, v ] = svd( h );
38 rotation = v * u'
39
40 ## reflection? theres more to that.
41 if ( det( rotation ) < 0 )
42 printf( "warning: det(r) < 0\n" );
43 if ( any( s( : ) ) < 0 )
44 printf( "found reflection, correcting.\n" );
45 v( :, 3 ) = -v( :, 3 );
46 rotation = v * u';
47 else
48 printf( "error: single-value-decomposition failed! \
49 provided data seems is too noisy for least-squares\n." );
50 endif
51 endif
52
53 ## 3) compute translation.
54 translation = centroid_q - ( rotation * centroid_p' )';
55
56 endfunction

```

A.3.4 Affine Transformation: affine.m

```

1#!/bin/octave
2function [ affine_rotation, translation, s ] = affine( p, q )
3## this function "affine(p,q)" finds the optimal affine transform in
4## 3-dimensional euclidian space, using least squares and
5## single-value-decomposition. Given a 3xn matrix (set of n 3d
6## positions), it returns and the rotation matrix "affine_rotation",
7## and the translation vector "translation".
8##
9## K. S. Arun, T. S. Huang and S. D. Blostein, "Least-Squares Fitting of
10## Two 3-D Point Sets," in IEEE Transactions on Pattern Analysis and
11## Machine Intelligence, vol. PAMI-9, no. 5, pp. 698-700, Sept. 1987,
12## doi: 10.1109/TPAMI.1987.4767965.
13##
14## Berthold K. P. Horn, "Closed-form solution of absolute orientation
15## using unit quaternions," J. Opt. Soc. Am. A 4, 629-642 (1987)
16##
17## @ moritz siegel
18
19 global hd
20 global wd

```

```

21 global nwd
22
23 ## check stuff.
24 assert( nargin == 2 && size( p ) == size( q ), ...
25     "need 2 identical input matrices\n" );
26 assert( size( p, 2 ) == 3, "input matrix p must be nx3\n" );
27 assert( size( q, 2 ) == 3, "input matrix q must be nx3\n" );
28 n = size( p, 1 );
29 assert( n > 2, "need at least 3 points\n" );
30
31 ## 1) center to get rid of translation.
32 centroid_p = mean( p, 1 );
33 centroid_q = mean( q, 1 );
34 p_shifted = p - repmat( centroid_p, n, 1 );
35 q_shifted = q - repmat( centroid_q, n, 1 );
36
37 ## 2) orthogonal reduction.
38 ## -----
39
40 ## variance (?) matrices.
41 s_p = p_shifted' * p_shifted;
42 s_q = q_shifted' * q_shifted;
43
44 ## square-roots of the covariance matrices.
45 ## choleski decomposition: "A -> LL*" , any advantage over sqrtm()?
46 #s_sqrt_p = sqrtm( s_p );
47 #s_sqrt_q = sqrtm( s_q );
48 s_sqrt_p = chol( s_p, "lower" );
49 s_sqrt_q = chol( s_q, "lower" );
50
51 ## left division. "x\y" is conceptually equivalent to the expression
52 ## "inv(x) * y" but it is computed without forming the inverse of x.
53 ## if the system is not square, or if the coefficient matrix is
54 ## singular, a minimum norm solution is computed.
55 p_orthogonal = ( s_sqrt_p \ p_shifted' )';
56 q_orthogonal = ( s_sqrt_q \ q_shifted' )';
57
58 ## "p" and "q" are now solely related by a rotational matrix
59 ## "r = s_inv_sqrt_q * affine * s_sqrt_p" (no inverse!).
60
61 ## 3) solve least squares problem for best rotation.
62 ## -----
63
64 ## covariance matrix again.

```

```

65 h = p_orthogonal' * q_orthogonal;
66
67 ## singular value decomposition.
68 [ u, s, v ] = svd( h );
69 rotation = v * u';
70
71 ## reflection? theres more to that.
72 if ( det( rotation ) < 0 )
73     printf( "warning: det(rotation) < 0\n" );
74     if ( any( s( : ) ) < 0 )
75         printf( "found reflection, correcting.\n" );
76         v( :, 3 ) = - v( :, 3 );
77         rotation = v * u';
78     else
79         printf( "error: single-value-decomposition might have failed! \
provided data seems is too noisy for least-squares.\n" );
80     endif
81 endif
82
83
84 ## 4) reverse the rotation to the non-orthogonal affine transform using
85 ## right division: "x/y" is conceptually equivalent to the expression
86 ## "x * inv(y)" but it is computed without forming the inverse of x.
87 affine_rotation = ( s_sqrt_q * rotation ) / s_sqrt_p;
88
89 ## 5) compute translation.
90 translation = centroid_q - ( affine_rotation * centroid_p' )';
91
92 ## save stuff for plotting.
93 ## chdir( cwd )
94 ## save p_shifted.mat p_shifted;
95 ## save q_shifted.mat q_shifted;
96 ## save p_orthogonal.mat p_orthogonal;
97 ## save q_orthogonal.mat q_orthogonal;
98 ## save rotation.mat rotation
99 ## save affine_rotation.mat affine_rotation
100 ## save translation.mat translation
101
102 endfunction

```

A.3.5 Clustering: dbSCAN.m

```

1 #!/bin/octave
2 ## This repository contains a simple implementation of DBSCAN algorithm

```

```

3  ## using GNU OCTAVE. DBSCAN is a popular clustering algorithm. It
4  ## creates clusters on a spatial data depending on two parameters:
5  ## MinPoints: minimum number of points needed in its neighbourhood to
6  ## consider it as a valid data(not noise). EPS: A distance on which
7  ## neighbourhood is calculated.
8  ## For more info:
9  ## https://github.com/devil1993/DBSCAN
10 ## https://en.wikipedia.org/wiki/DBSCAN
11 ##
12    ↵ http://citeseerx.ist.psu.edu/viewdoc/download;jsessionid=1A6A7A85AF3F43BCBF66D847FEC8F8
13 function [assignments,C] = dbscan(X,minpts,EPs)
14 C = 0;
15 assignments = zeros(size(X)(1),1);
16 clustered = zeros(size(X)(1),1);
17 for i=1: size(X)(1)
18   if(clustered(i)==1)
19     continue;
20   endif
21   clustered(i)=1;
22   isneighbour = [];
23   neighbourcount = 0;
24   for j=1: size(X)(1)
25     dist = sqrt(sum((X(i,:)-X(j,:)).^2));
26     if(dist<EPs)
27       neighbourcount++;
28       isneighbour = [isneighbour j];
29     endif
30   endfor
31   if(neighbourcount<minpts)
32     continue;
33   else
34     C++;
35     assignments(i) = C;
36     for k=isneighbour
37       if(clustered(k)==0)
38         clustered(k) = 1;
39         _isneighbour = [];
40         _neighbourcount = 0;
41         for j=1: size(X)(1)
42           dist = sqrt(sum((X(k,:)-X(j,:)).^2));
43           if(dist<EPs)
44             _neighbourcount++;
45             _isneighbour = [_isneighbour j];
46           endif

```

```
46
47     if(_neighbourcount>=minpts)
48         isneighbour = [isneighbour _isneighbour];
49     endif
50
51     assignments(k) = C;
52
53     endif
54
55 endfunction
```

A.3.6 Simulate Dual Colour 3d SMLM Data: simulate.m


```
65 | case "rigid"
66 |     [ rekovered_transform, rekovered_translation ] = rig( p, q );
67 | case "affine"
68 |     [ rekovered_transform, rekovered_translation ] = affine( p, q );
69 | endswitch
70 |
71 | if ( any( any( ( simulated_transform - rekovered_transform ) > eps ) ) )
72 |     disp( "warning: failed to recover affine transform" );
73 | endif
```

Bibliography

- [np1,] The nobel prize in chemistry 2014. nobelprize.org. nobel prize outreach ab 2023. sun. 5 feb 2023.
- [Arun et al., 1987] Arun, K. S., Huang, T., and Blostein, S. D. (1987). Least-squares fitting of two 3-d point sets. *IEEE Transactions on Pattern Analysis and Machine Intelligence*, PAMI-9:698–700.
- [Bley et al., 2022] Bley, C. J., Nie, S., Mobbs, G. W., Petrovic, S., Gres, A. T., Liu, X., Mukherjee, S., Harvey, S., Huber, F. M., Lin, D. H., Brown, B., Tang, A. W., Rundlet, E. J., Correia, A. R., Chen, S., Regmi, S. G., Stevens, T. A., Jette, C. A., Dasso, M., Patke, A., Palazzo, A. F., Kossiakoff, A. A., and Hoelz, A. (2022). Architecture of the cytoplasmic face of the nuclear pore. *Science*, 376(6598):eabm9129.
- [Chao et al., 2016] Chao, J., Ward, E. S., and Ober, R. J. (2016). Fisher information theory for parameter estimation in single molecule microscopy: tutorial. *J. Opt. Soc. Am. A*, 33(7):B36–B57.
- [Ester et al., 1996] Ester, M., Kriegel, H.-P., Sander, J., and Xu, X. (1996). A density-based algorithm for discovering clusters in large spatial databases with noise. pages 226–231. AAAI Press.
- [Heilemann et al., 2008] Heilemann, M., van de Linde, S., Schüttelpehl, M., Kasper, R., Seefeldt, B., Mukherjee, A., Tinnefeld, P., and Sauer, M. (2008). Subdiffraction-resolution fluorescence imaging with conventional fluorescent probes. *Angewandte Chemie*, 47 33:6172–6.
- [Nahidiazar et al., 2016] Nahidiazar, L., Agronskaia, A. V., Broertjes, J., van den Broek, B., and Jalink, K. (2016). Optimizing imaging conditions for demanding multi-color super resolution localization microscopy. *PLOS ONE*, 11(7):1–18.
- [Nschlöe, 2023] Nschlöe (accessed 13.01.2023). [wikipedia.org/wiki/File:Zernike_polynomials_with_read-blue_cmap.png](https://en.wikipedia.org/wik.../Zernike_polynomials_with_read-blue_cmap.png).
- [Ovesný et al., 2014] Ovesný, M., Křížek, P., Borkovec, J., Švindrych, Z., and Hagen, G. M. (2014). ThunderSTORM: a comprehensive ImageJ plug-in for PALM and STORM data analysis and super-resolution imaging. *Bioinformatics*, 30(16):2389–2390.
- [Qu et al., 2010] Qu, J., Gong, L., and Yang, L. (2010). A 3d point matching algorithm for affine registration. *International Journal of Computer Assisted Radiology and Surgery*, 6(2):229–236.
- [Siegel, 2021] Siegel, M. (2021 (accessed June 30, 2021)). Repository for my biophysics project thesis. <https://github.com/imrahilias/biophysics>.
- [SMLM, 2021] SMLM (accessed June 30, 2021). <https://biophysics.iap.tuwien.ac.at/research/smlm/>.

[Zelger et al., 2018] Zelger, P., Kaser, K., Rossboth, B., Velas, L., Schütz, G. J., and Jesacher, A. (2018). Three-dimensional localization microscopy using deep learning. *Opt. Express*, 26(25):33166–33179.

List of Tables

3.1	Ingredients used for preparation of OxEA buffer for dual colour dSTORM.	14
4.1	Quality of the recovered rotation translation vectors (transformation) matrices $\mathbf{t}_{s,r,a}^{r,a}$	40
4.2	Quality of the recovered rotation (transformation) matrices $\mathbf{R}_{s,r,a}^{r,a}$	40

List of Figures

1.1	Jablonski diagram including vibrational levels for absorbance, non-radiative decay, and fluorescence. Obtained under CC0 license from	6
1.2	Influence of imaging parameters on the reconstructed SMLM image. The actual localization (left column) of the protein molecules (circles) yielding the obtained localization (right column), [SMLM, 2021].	8
2.1	The first 21 Zernike polynomials, ordered vertically by radial degree and horizontally by azimuthal degree, obtained under CC-BY-SA license from [Nschloe, 2023].	10
3.1	Blue channel ZERNIKE modes {1 ... 37, 56} versus aberrations of PSF model via phase retrieval, for all three correction collar settings (0.13, 0.17, 0.19).	16
3.2	Red channel ZERNIKE modes {1 ... 37, 56} versus aberrations of PSF model via phase retrieval, for all three correction collar settings (0.13, 0.17, 0.19).	17
3.3	Red and blue channel ZERNIKE modes {1 ... 37, 56} versus aberrations of PSF model via phase retrieval, for correction collar setting of 0.13.	18
3.4	Red and blue channel ZERNIKE modes {1 ... 37, 56} versus aberrations of PSF model via phase retrieval, for correction collar setting of 0.17.	19
3.5	Red and blue channel ZERNIKE modes {1 ... 37, 56} versus aberrations of PSF model via phase retrieval, for correction collar setting of 0.19.	20
3.6	Estimated CRAMÉR RAO lower bound for different correction Collar settings (varying linestyles for 0.13, 0.17, 0.19) of the Olympus 1.5 NA objective; for X, Y and Z axis (top, middle, and bottom); for both red and blue channel (colours). .	22
3.7	Estimated CRAMÉR RAO lower bound for blue light for different correction Collar settings (teal: 0.13, orange: 0.17, purple: 0.19) of the Olympus 1.5 NA objective; grouped by X, Y and Z axis (top, middle, and bottom).	23
3.8	Estimated CRAMÉR RAO lower bound for blue light for X, Y and Z axis (teal, orange and purple lines); grouped by different correction Collar settings (top: 0.13, middle: 0.17, bottom: 0.19) of the Olympus 1.5 NA objective.	23
3.9	Estimated CRAMÉR RAO lower bound for red light for different correction Collar settings (teal: 0.13, orange: 0.17, purple: 0.19) of the Olympus 1.5 NA objective; grouped by X, Y and Z axis (top, middle, and bottom).	24

3.10	Estimated CRAMÉR RAO lower bound for red light for X, Y and Z axis (teal, orange and purple lines); grouped by different correction Collar settings (top: 0.13, middle: 0.17, bottom: 0.19) of the Olympus 1.5 NA objective.	24
3.11	Example overview of a set of two dimensional SMLM data of NPCs, the labeled NPC tori are clearly visible.	25
3.12	Zoom of Figure 3.11, Example of a set of two dimensional SMLM data of NPCs; The labeled NPC tori are clearly visible, even the more or less eight-fold symmetry of the nucleoporins is resolved.	25
3.13	Cytoplasmic face of the human NPC. Near-atomic composite structure of the NPC generated by docking high-resolution crystal structures into a cryo-ET reconstruction of an intact human NPC. The symmetric core, embedded in the nuclear envelope, is decorated with NUP358 (red) domains bound to Ran (gray), flexibly projected into the cytoplasm, and CFNCs (pink) overlooking the central transport channel. Figure and description from [Bley et al., 2022].	26
3.14	3d plot of all 370148 drift corrected localisations, colour coded by photon count.	27
3.15	histogram of the photon count for the localisations.	28
3.16	3d plot of all 154237 filtered localisations, colour coded by photon count.	28
3.17	3d plot of all 98456 filtered localisations, colour coded by photon count.	28
3.18	3d plot of the localisations of the 658 identified clusters (omitting 35489 localisations as noise, due to not belonging to a cluster), colour coded by photon count.	29
3.19	3d plot of the positions of the 451 filtered clusters, colour coded by photon count.	30
3.20	3d plot of the localisations within the 10 <i>best</i> clusters, colour coded by photon count.	30
3.21	3d plot of the localisations within the 10 <i>best</i> clusters, colour coded by cluster assignment.	30
3.22	histogram of the x,y (right) respective z distribution (left) of the localisations within the <i>best</i> cluster (top), the <i>worst</i> (bottom) and one in between.	31
3.23	Demonstration of the recovery of rigid (left) respective affine (right) transformations, via recovering localisations of simulated two channel SMLM data; transformation (magenta) from red channel (violet) to blue channel (cyan); for the use cases of translation (top), rigid transformation (middle) and affine transformation (bottom). Obviously a rigid transformation may not correctly reconstruct an affine transformed data set (bottom left).	34
3.24	Demonstration of a rigid transformation of the localisations (magenta \circ) from blue channel (blue \times) to red channel ($+$); the transformed blue channel localisations mostly align well with the red channel localisations.	36

Acronyms

CRLB CRAMÉR RAO lower bound. 11, 21

dSTORM direct stochastic optical reconstruction microscopy. 7, 9, 10, 12, 14, 25, 62

EMCCD Electron multiplying charge-coupled device. 7

FWHM full width half maximum. 7

Gloxy glucose oxidase dSTORM buffer. 9, 14, 25, 32, 39

MEA β -mercaptopropylamine hydrochloride. 10, 14

MLE maximum likelihood estimation. 9

NPC nuclear pore complex. 12, 14, 25, 27, 29–32, 38, 39

OxEA OxyFlour β -mercaptopropylamine hydrochloride dSTORM buffer. 10, 14, 32, 39

PBS phosphate-buffered saline. 10, 14

PSF point spread function. 7, 9, 11

RMS root mean square. 29, 38

SMLM single molecule localisation microscopy. 5–12, 14, 25, 27, 32, 34, 35, 37, 40, 64

SNR signal-to-noise ratio. 7, 14, 32, 39

STORM stochastic optical reconstruction microscopy. 9

SVD singular value decomposition. 11, 12

TIRF total internal reflection fluorescence. 7

Index

- RAYLEIGH shift, 5
- STOKES shift, 5
- aberration-free, 8
- aberrations, 9
- AF488, 13
- AF647, 13
- affine transform, 10
- Alexa Fluors, 13
- beads, 5, 9
- bleaching, 10
- bright state, 8
- buffers, 5
- calibration, 10
- catalase, 9
- centroid, 10
- Choleski decomposition, 11
- correction collar, 9
- covariance matrices, 11
- Cramér Rao lower bound, 10
- diffraction limit, 4
- drift, 10, 26
- dSTORM microscopy, 8
- euclidean space, 11
- evanescent field, 6
- evanescent wave, 6
- expectation values, 8
- fluorescence microscopy, 4
- fluorophore blinking, 13
- fluorophores, 4, 5
- fminunc, 8
- Gaussian, 7
- gaussian fit, 11
- Gloxy buffer, 8
- glucose, 8
- glucose oxidase, 8
- ground state, 4
- histogram, 29
- ImageJ, 11, 24
- In-focus, 24
- inter-system crossing, 5
- inverse FISHER information matrix, 10
- inverse Fisher information matrix, 10
- Jupyter Notebook, 26
- least squares, 10
- lifetime, 5
- MATLAB, 8
- maximum likelihood estimation, 8
- mercaptoethylamine hydrochloride, 9
- negative log-likelihood function, 8
- Noll coefficients, 8
- nucleoporin, 24
- Octave, 11
- Olympus objective, 9
- orthogonal reduction, 11
- OxEA buffer, 9
- OxyFlour, 9
- parameter vector, 8
- particle tracking, 31

phase retrieval, 9
phosphate-buffered saline, 9
phosphorescence, 5
photobleaching, 5, 8
photoswitching, 8
point spread function model, 8
Poissonian probability distribution, 8
Python, 26

rate, 5
resolution, 4
rigid transform, 10

scaling, 10
shearing, 10
single molecule localisation, 6
singular value decomposition, 10
sodium DL-lactate, 9
spherical aberration, 8
storm buffer, 8
super resolution, 4

ThunderSTORM, 11
total internal reflection, 6
tracking, 27
triplet, 5

vibrational states, 4

x,y precision, 24

Zernike modes, 8

index